A BOLOMETRIC TECHNIQUE FOR BROADBAND MEASUREMENT OF SURFACE RESISTANCE AND APPLICATION TO SINGLE CRYSTAL $YBa_2Cu_3O_{6.99}$

By

Patrick J. Turner

B. Sc. McMaster University, 1997

A THESIS SUBMITTED IN PARTIAL FULFILLMENT OF

THE REQUIREMENTS FOR THE DEGREE OF

MASTER OF SCIENCE

in

THE FACULTY OF GRADUATE STUDIES

DEPARTMENT OF PHYSICS AND ASTRONOMY

We accept this thesis as conforming

to the required standard

THE UNIVERSITY OF BRITISH COLUMBIA

October 1999

© Patrick J. Turner, 1999

In presenting this thesis in partial fulfilment of the requirements for an advanced degree at the University of British Columbia, I agree that the Library shall make it freely available for reference and study. I further agree that permission for extensive copying of this thesis for scholarly purposes may be granted by the head of my department or by his or her representatives. It is understood that copying or publication of this thesis for financial gain shall not be allowed without my written permission.

Department of Physics and Astronomy
The University of British Columbia
6224 Agricultural Road
Vancouver, B.C., Canada
V6T 1Z1

Date: Oct. 15, 1999

Abstract

A bolometric technique has been developed to measure the frequency dependence of the surface resistance, R_s, of high temperature superconductor single crystals near 1K over the range 0.1 to 20 GHz. This experiment measures the shape of the conductivity spectrum, while also having the sensitivity to measure the residual loss in the low temperature limit. Preliminary measurements on detwinned ultrahigh purity single crystals of $YBa_2Cu_3O_{6.95}$ reveal that the real part of the conductivity $\sigma_1(\omega)$ is reasonably well fit by a Drude model over the majority of the frequency range. Variations between measurements have been observed which raise questions about the stability and contamination of YBCO crystal surfaces. Given that the conductivity spectrum has a width of about 7 GHz, it is natural to expect that the mechanism involved will settle into a low T limit when T is below 7GHz = 0.35K (=7 GHz×h/k_B). Work towards performing the experiment at 0.1K is in progress.

Table of Contents

List of Figures

Acknowledgements

It has been a great pleasure to have had the opportunity to work with Walter Hardy. His expertise, patience, and insight combine to make an outstanding physicist and supervisor. I have also benefitted from and enjoyed the guidance of Doug Bonn over the past two years.

The bolometry experiment presented in this thesis has involved past and present members of the lab and their efforts must be acknowledged: David Morgan and John Preston for work before I arrived at UBC, Mike Hayden from whom I learned a great deal as we worked together on this experiment, Ruixing Liang for such fine YBCO crystals, and Saeid Kamal for his many contributions and continuous interest in this work.

I would like to thank the guys in the lab: Chris Bidinosti, Pinder Dosanjh, Ahmad Hosseini, Richard Harris, Saeid Kamal, and Ruixing Liang for being such fine friends, teachers, and people. This thesis has benefitted greatly from the editorial efforts of Richard Harris, Saeid Kamal and Ahmad Hosseini.

I would also like to thank my friends and particularly my family for their support over the years.

Finally, a warm thanks to my wife Holly whose patience, encouragement, and companionship every step of the way has made all the difference.

Chapter 1

Introduction

Discovered by Bednorz and Müller in 1986[1], high temperature superconductivity (HTSC) has remained a topic of considerable interest and effort in the scientific and engineering community. This is due in part to the possibilities for commercial application because of higher critical temperatures, and in part to the lack of an explanation for their remarkable physical behaviour. For the scientist, the most pressing issue is that there is no consensus on a mechanism which explains the anomalous properties of the cuprate superconductors in both the normal state and the superconducting state.

The occurrence of superconductivity in the cuprates is thought to be intimately linked with the two dimensional nature of the materials. The parent compounds are antiferromagnetic insulators which display superconductivity when sufficiently doped with holes. The material under study in this thesis has an orthorhombic crystal structure with highly anisotropic transport properties. Each unit cell of $YBa_2Cu_3O_{7-\delta}$ contains a pair of copper oxide (CuO_2) planes perpendicular to the $\hat{c}$-axis, and a layer of CuO chains running in the $\hat{b}$-direction. The superconducting properties are thought to be dominated by the planes, with the chains acting as charge reservoirs that control the carrier density in the planes[2]. The chains are not believed to be necessary for superconductivity, and are generally considered to be a nuisance to experimentalists. However, through the study of the ab-plane anisotropy in untwinned crystals one can try to understand the influence of the chains.

A result of the complex stoichiometry of the cuprate superconductors is that the

interpretation of experiments must be approached with caution. In particular, it can be difficult to ascertain whether experiments are probing intrinsic properties of the system which reflect the physical nature of the superconductivity, or whether one is simply observing extrinsic effects. It is important therefore to approach the problem with a number of different experimental methods and to try to construct a consistent physical picture. For this reason it has been difficult and time consuming for the HTSC community to reach a consensus on the experimental results.

The explanation of conventional superconductivity is intimately linked with the existence of a full or s-wave energy gap at the Fermi surface. In an effort to understand unconventional superconductivity, a common starting point has been to revisit conventional superconductors which were discovered in 1911 by Onnes[3] and explained by BCS theory in 1957[4]. Hence the most widely discussed microscopic models of unconventional superconductivity have their origins in the language of BCS theory.

One of the first striking dissimilarities with the unconventional superconductors is the existence of nodes in the energy gap function. Despite the initial experimental claims to have observed the signature of a full s-wave gap in HiT_c materials, a convincing set of independent measurements have since established the existence of predominantely d-wave symmetry. Perhaps the strongest evidence for a d-wave density of states comes from Josephson junction DC SQUID rings which examine the phase effects between s-wave and d-wave superconductors[5, 6]. The microwave contribution to this understanding came early on with the measurement of a linear temperature dependence of the magnetic penetration depth $\lambda(T)$ by Hardy *et al.* which was one of the first experiments to provide evidence of the gap nodes[7].

While an intimate knowledge of the microwave conductivity will not *explain* unconventional superconductivity, it will most certainly shed light upon some of the key issues

at the heart of the debate. Microwave surface impedance of unconventional superconductors yields information about the pairing mechanism and the excitations from the superconducting groundstate. The exact form of the conductivity $\sigma(\omega)$ can in principle be calculated from a microscopic theory of superconductivity, and hence its measurement provides an important constraint for theorists.

1.1 Motivation for Experiment

While a considerable effort has been made by a number of groups to measure the microwave surface impedance of cuprates over a wide range of temperature and frequency, one area which has remained undertested due to technological difficulties with experiments is the T$\rightarrow$0 limit. Along with the establishment of d-wave gap nodes in the cuprates came the realization that the low temperature behaviour of the conductivity would be very sensitive to the nature of these nodes. A novel feature which accompanies the presence of the nodes is the existence of T=0 quasiparticles which will contribute to low temperature transport.

Recent measurements at UBC by Hosseini *et al.* on the microwave surface impedance of ultra-high purity single crystals of YBCO have confirmed their earlier suggestions that the quasiparticle scattering rate $1/\tau$ is nearly temperature independent below 20 K[8]. This is the first time that enough data has been obtained on a single sample in which both the temperature and frequency dependence can together convincingly support this notion. They conclude that the effects of elastic impurity scattering will dominate the low temperature transport, and that the conductivity spectrum will be sensitive to the detailed nature of the scattering mechanism. The theoretical interpretation of the scattering remains debatable and the fact that at low temperature $1/\tau$ does not depend on energy is inconsistent with standard simple pictures of impurity scattering for a d-wave

superconductor[9]. This has prompted the reevaluation of existing theories of conductivity in d-wave superconductors drawing increased attention to predictions for the T→0 limit[9, 10, 11].

The past decade of work on HTSC has seen widespread debate over the implications of d-wave gap nodes on the dynamics of low temperature quasiparticles. One key prediction is that the T→0 limit will see the onset of universal transport where the quasiparticle transport becomes independent of the scattering rate[12]. The explanation for this is based on the presence of a band of impurity states which reside near the nodes. Part of the initial motivation for the development of this broadband measurement technique was to test the universal limit which suggests the T→0, $\omega \rightarrow 0$ conductivity value of $\sigma_{oo} = ne^2/(m\pi\Delta_o)$ where Δ_o is the maximum gap width. Microwave surface impedance measurements down to 1.2 K to date have not been able to confirm or deny this value, however they seem to point towards T→0 extrapolations which are larger than σ_{oo}[11]. On the other hand, Taillefer *et al.* have measured the thermal conductivity counterpart in 5 YBCO single crystals with varying levels of Zn (0-3%) doping[13]. They observe a quasiparticle thermal conductivity in these 5 crystals at 100 mK which is independent of Zn concentration, although roughly double the predicted value. This universality remains to be carefully examined in the microwave frequency range.

The initial work on the broadband microwave technique for the measurement of cuprate superconductors began about five years ago. Measurements around that time by Bonn *et al.* at UBC indicated a quasiparticle scattering rate on the order of 10GHz[14]. Hence the measurement of σ_1 over the frequency band of 0-20 GHz was chosen to ensure the measurement of the bulk of the superconducting state spectral weight.

1.2 Microwave Surface Impedance

The microwave surface impedance of a material is defined to be the ratio of the tangential electric and magnetic fields at the conducting surface. In a rectangular coordinate system where an isotropic conductor fills the half space $z \leq 0$, the complex surface impedance is given by

$$Z_s = \left(\frac{E_x}{H_y}\right)_{z=0} = R_s + \imath X_s. \tag{1.1}$$

In an applied H field, this corresponds physically to the ratio of the induced electric field which drives the screening current, to the magnetic field which sets the total current required for screening. When a conductor is placed in an AC magnetic field, the Faraday effect requires that screening currents flow in a manner which tends to cancel the applied field. When the conductivity is sufficiently high, the screening currents are restricted to the surface of the material, while the interior of the conductor remains field free. The units of Z_s are ohms; the real part, R_s, is called the surface resistance and the imaginary part, X_s, the surface reactance. As will be seen shortly, it is R_s which determines the power absorption of a conductor in an AC field.

The interpretation of the behaviour of conductive materials at microwave frequencies is straightforward in the case of local electrodynamics. With the cuprate superconductors, the local limit assumption is generally valid in both the normal and superconducting state. The justification for this lies in the fact that these materials are quasi 2-dimensional[15]. Within this scenario, the relatively small values for both the coherence length, ξ and ℓ in the superconducting state as well as ℓ above the transition temperature T_c in the normal state guarantee that non-local corrections will be small for the measurement geometry used by this experiment[16].

When local electrodynamics are valid, Ohm's law applies and the local current density

is proportional to the local electric field

$$\mathbf{J} = \sigma \mathbf{E}. \tag{1.2}$$

Omitting the displacement current which is negligible in good conductors at not too high frequencies (*i.e.* when $\sigma \geq \omega\epsilon$), Maxwell's equations read

$$\begin{aligned} \nabla \times \mathbf{E} &= -\mu \frac{\partial \mathbf{H}}{\partial t} && (1.3) \\ \nabla \times \mathbf{H} &= \mathbf{J}. && (1.4) \end{aligned}$$

These equations lead to the wave equation

$$\nabla^2 \mathbf{H} = -\mu_o \sigma \frac{\partial \mathbf{H}}{\partial t} \tag{1.5}$$

where the conductor has been taken as non magnetic (*i.e.* $\mu = \mu_o$).

In the semi-infinite geometry described earlier, with a uniform harmonic magnetic field applied along the y axis, the wave equation is

$$\frac{d^2 H}{dz^2} = -\imath \mu_o \sigma \omega H_y = -k^2 H_y. \tag{1.6}$$

With the requirement that the field amplitude not diverge anywhere, the solutions are

$$\begin{aligned} E_x(z,t) &= E_{xo} e^{-\imath kz + \imath \omega t} \\ H_y(z,t) &= H_{yo} e^{-\imath kz + \imath \omega t} && (1.7) \\ H_{yo} &= \frac{k}{\mu_o \omega \imath} E_{xo} \end{aligned}$$

where H_{yo} is the field amplitude outside the conductor. The propagation constant k obeys

$$k = \sqrt{\imath \mu_o \, \omega \sigma} = \sqrt{\frac{\mu_o \, \omega \sigma}{2}} (1 + \imath). \tag{1.8}$$

This leads to the definition of the classical skin depth $\delta = \sqrt{\frac{2}{\mu_o \omega \sigma}}$ which is the length scale over which the fields decay exponentially with distance into the conductor. From 1.7 and 1.8 it is clear that the surface impedance 1.1 is thus

$$Z_s = \frac{E_{xo}}{H_{yo}} = \sqrt{\frac{\imath \mu_o \omega}{\sigma}}. \tag{1.9}$$

In the case of a normal metal, the conductivity is purely real (as long as $\sigma \gg \omega\epsilon$) and the surface resistance and reactance are equal. The surface impedance then takes the form

$$\begin{aligned} Z_s &= R_s + \imath X_s \\ &= \sqrt{\frac{\mu_o \omega}{2\sigma}}(1 + \imath.) \end{aligned} \tag{1.10}$$

In the general case, the conductivity is taken as complex, $\sigma = \sigma_1 - \imath\sigma_2$, reflecting the resistive and inductive behaviour of the conductor in AC fields. With this the surface resistance is found to be

$$R_s = \sqrt{\frac{\mu_o \omega (\sqrt{\sigma_1^2 + \sigma_2^2} - \sigma_2)}{2(\sigma_1^2 + \sigma_2^2)}}. \tag{1.11}$$

When in the normal state, a superconductor displays metallic behaviour and the surface impedance is given by 1.10. As the temperature is lowered below T_c as a consequence of the apearance of "superconducting electrons" σ_2 quickly becomes much larger than σ_1. With $\sigma_2 \gg \sigma_1$, the propagation constant takes the approximate form $k = \imath\sqrt{\mu_o \omega \sigma_2}$ and the magnetic field is then seen to decay exponentially over a length scale called the magnetic penetration depth,

$$\lambda = \frac{1}{\sqrt{\mu_o \omega \sigma_2}} \tag{1.12}$$

and the surface resistance 1.11 can be simplified to

$$R_s = \frac{1}{2}\mu_o^2 \omega^2 \lambda^3 \sigma_1. \tag{1.13}$$

Equations 1.12 and 1.13 demonstrate that the quantities R_s and λ provide access to the real and imaginary parts of the conductivity of a superconductor. We note that σ_2 is obtained directly from a measurement of λ, but both λ and R_s are needed to extract σ_1.

1.3 Power Absorption

For either a metal or a superconductor in an electromagnetic field, the total absorbed power per unit square area can be calculated by finding the real part of the complex Poynting vector at the surface, *i.e.*

$$Re(S_{zo}) = Re(\frac{1}{2}E_{xo} \times H^*_{yo}). \tag{1.14}$$

With the substitution of equation 1.7, this becomes

$$Re(S_{zo}) = Re(\frac{1}{2}ZH^2_{yo}). \tag{1.15}$$

A straightforward integration of Ampere's law demonstrates that the tangential magnetic field at the surface is equal to the total surface current per unit width[1]

$$J_{so} = H_{yo}. \tag{1.16}$$

The total power absorbed per unit area is therefore

$$\begin{aligned} Re(S_{zo}) &= Re(\frac{1}{2}Z_sJ^2_{so}) \\ &= \frac{1}{2}R_sJ^2_{so} \end{aligned} \tag{1.17}$$

which is readily recognized as an ohmic loss per unit area.

[1]See appendix A.

1.4 Two Fluid Model Interpretation

A generalized phenomenological 2-fluid model is a useful approach when discussing the microwave conductivity of superconductors. This oversimplified picture of superconductivity is useful as a framework for interpreting electromagnetic behaviour while avoiding the complications of a more realistic microscopic theory. Here the notation of Tinkham is adopted[2].

The 2-fluid idea arises from the fact that a superconductor exhibits behaviour characteristic of the presence of both a normal electron fluid and a superconducting electron fluid. A classical picture of electron transport is used for each fluid by combining Newton's Laws, Ohm's Law, and a relaxation time τ resulting from scattering. It is furthermore assumed that these two fluids are noninteracting. The current density is given by $\mathbf{J} = ne\mathbf{v}$ where e and n are the electron charge and density respectively and $\mathbf{v}$ is the electron drift velocity for the fluid in question. In the presence of an applied electric field, the current density obeys

$$\frac{d\mathbf{J}}{dt} = \frac{ne^2\mathbf{E}}{m^*} - \frac{\mathbf{J}}{\tau}. \tag{1.18}$$

Assuming sinusoidal time variation of the incident field, and that Ohm's law 1.2 holds, 1.18 is solved to yield the real and imaginary parts of the conductivity

$$\begin{aligned} \sigma_1(\omega) &= \sigma_o \frac{1}{1+\omega^2\tau^2} \\ \sigma_2(\omega) &= \sigma_o \frac{\omega\tau}{1+\omega^2\tau^2} \\ \sigma_o &= \frac{ne^2\tau}{m^*}. \end{aligned} \tag{1.19}$$

This has assumed that the response of the material to the field is linear, *i.e.* that no other frequency harmonics are excited by the field.

Within the 2-fluid model, the normal and superfluid electrons are considered as parallel mechanisms for conduction so that $\sigma_1(\omega)$ and $\sigma_2(\omega)$ in Eq. 1.19 each become the sum

of two contributions, one from the normal fluid and one from the superfluid. In the case of the normal electrons, the conductivity $\sigma_n(\omega)$ is as stated in 1.19, with $n \rightarrow n_n$ where the subscript denotes normal fluid. For the treatment of the superfluid, the lossless DC conduction is accommodated by the model by letting $\tau \rightarrow \infty$. In this case 1.19 $\sigma_{1s}(\omega)$ becomes a delta-function at $\omega = 0$ having oscillator strength (n_s/m^*). The imaginary part $\sigma_{2s}(\omega)$ simplifies to $\left(\frac{ne^2}{m^*\omega}\right)$. Thus the real and imaginary parts of $\sigma(\omega) = \sigma_s(\omega) + \sigma_n(\omega)$ yields

$$\begin{aligned} \sigma_1(\omega) &= \frac{\pi n_s e^2}{m^*}\delta(\omega) + \frac{n_n e^2}{m^*}\left(\frac{\tau}{1+\omega^2\tau^2}\right) \\ \sigma_2(\omega) &= \frac{n_s e^2}{m^*\omega} + \frac{n_n e^2}{m^*}\left(\frac{\omega\tau^2}{1+\omega^2\tau^2}\right). \end{aligned} \tag{1.20}$$

The real part of the conductivity contains both the $\omega = 0$ delta-function contribution from the superfluid, and the normal fluid Drude spectrum. Since σ_1 describes absorption, the appearance of the delta-function at first seems out of place. However, the spectral weight which resides in the delta-function can be attributed to the energy absorbed in accelerating the non-dissipative superfluid. The delta-function is also required in order that the Kramers-Kronig relations between $\sigma_1(\omega)$ and $\sigma_2(\omega)$ be obeyed.

As dictated by a general oscillator strength sum rule, the value of $\int_0^\infty \sigma_1(\omega)d\omega$ is a conserved quantity. Hence the spectral weight is shifted between the normal and superfluid as the temperature is varied. If a superconductor has all of the electrons condensed into the superfluid at T=0, then it is said to be in the clean limit and obeys

$$\frac{n_n e^2}{m_n^*}(T) + \frac{n_s e^2}{m_s^*}(T) = \frac{n_s e^2}{m_s^*}(T = 0) \tag{1.21}$$

As temperature is increased, quasiparticles are thermally excited and the Drude term in $\sigma_1(\omega, \tau)$ builds at the expense of the strength of the delta-function. For $T > T_c$, the superfluid fraction is reduced to zero.

It is clear that the measurement of $\sigma_1(\omega, T)$ for $\omega > 0$ provides information about both the thermally excited quasiparticles as well as the superfluid delta-function. From 1.20 it can be seen that when the frequency is no too high ($\omega\tau \ll 1$), σ_2 simplifies to

$$\sigma_2(\omega) = \frac{e^2}{m^*\omega}(n_s + n_n\omega^2\tau^2). \tag{1.22}$$

Hence at low frequency, the behaviour of σ_2 is dominated by the superfluid as long as the first term in 1.22 is much greater than the second. This is is the case over a wide temperature range extending very near to T_c where n_s diminishes rapidly. From 1.12 it is seen that the physical quantity λ is determined by σ_2, and is therefore a measure of the superfluid density. 1.20 yields the relation

$$\sigma_2(\omega) = \frac{n_s e^2}{m^*\omega} = \frac{1}{\mu_o\omega\lambda^2(T)}. \tag{1.23}$$

This provides another experimental opportunity to access the delta-function oscillator strength which appears in the expression for σ_1. Furthermore since it has been assumed that the system is in the clean limit, the superfluid fraction can be written as

$$n_s = \frac{n_s(T)}{n_o} = \frac{\lambda^2(0)}{\lambda^2(T)}. \tag{1.24}$$

Experimental methods which have proven useful in the measurement of λ for HTSC single crystals include Fourier transform infrared reflectivity (FTIR) spectroscopy, muon spin relaxation (μsr) and field volume exclusion[17]. Perhaps the most successful of these in measuring the small temperature dependence of λ has been the microwave cavity perturbation technique which measures the change in apparent volume of a superconducting resonator due to the field exclusion of a superconducting sample[7]. As the sample is heated from the base temperature T_o, shifts in the cavity resonant frequency are related to $\Delta\lambda$. In our lab T_o=1.2 K, so that for HiT_c samples with T_c of order 50 to 100 K, $\lambda(T_o) \simeq \lambda(0)$. The drawback with measurements of this type is that the absolute value

of the penetration depth, λ_o, is not obtainable, partly because the volume of the sample cannot be measured with high enough precision and partly because of uncertainty in other calibration factors. It is however possible to extract λ_o from FTIR spectroscopy measurements (see for example Basov *et al.*[18]). μsr measurements are also absolute, however they do not independently measure λ_a and λ_b, but rather an average of the two[19]. Experimental numbers for the value of λ_o are of great importance if $\sigma_1(\omega)$ is to be properly extracted from R_s measurements.

Chapter 2

Experimental Approach

While high precision microwave cavity perturbation techniques for the measurement of $R_s(T)$ in HTSC superconductors over a wide temperature range (1-300K) have been developed over the past decade, they are restricted to a single frequency mode of operation[17]. This means that data from a number of different experiments must be pieced together in order to build up a picture of the frequency dependence. This approach has been used by Hosseini *et al.* to provide a reasonable picture of the microwave conductivity spectrum using 5 frequencies between 1 and 75 GHz[8]. However, due to difficulties with absolute calibrations and non-perturbative effects, the error bars on the low temperature data remain significant and hence the detailed shape of the conductivity spectrum remains somewhat uncertain. A single broadband measurement of this spectrum would be able to confirm these measurements, as well as provide a more detailed picture.

The goal of this work is the measurement of the *frequency* dependence of the low temperature limit of the microwave conductivity $\sigma_1(\omega)$ in single crystal HTSC superconductors. This is a challenging measurement due to the very low microwave loss in high quality crystals and the requirement of a broadband measurement which makes well established cavity perturbation methods inappropriate. In order to meet these challenges, a bolometric measurement technique has been developed whereby the power dissipated by a superconducting sample in a microwave frequency magnetic field is measured via the heating of the sample. The dissipation for a YBCO crystal measured in this experiment is rather small, typically a fraction of a nW at low microwave frequency. To

improve the signal to noise ratio, a phase-sensitive approach to the measurement is taken in which the microwave power which heats the sample is modulated as $1 + \cos(\omega t)$ and the induced temperature oscillations in the sample at frequency ω are measured with a lock-in amplifier. For this work, a modulation frequency of f=0.45Hz was used for reasons which will be explained in section 2.4. As pointed out in the previous chapter, it is R_s which determines the power dissipation of a conductor in a microwave field and hence the temperature response is directly related to R_s of the superconductor. Detection of the small temperature modulation requires highly sensitive thermometers, which so far has restricted the operation of this experiment to a narrow temperature range near 1 K. This chapter introduces the apparatus and explains its operation. The final section describes the ultra-high purity YBCO crystals which have been studied.

2.1 The Terminated Coaxial Transmission Line

The continuous frequency measurement of $R_s(\omega)$ requires a frequency tuneable and spatially uniform magnetic field over a reasonably wide microwave band. The variable frequency requirement motivated the employment of a nonresonant technique. A shorted coaxial transmission line was chosen since it supports a TEM mode with a magnetic field antinode and electric field node at the shorted end. Standard 0.141" O.D. stainless steel semi-rigid coaxial line with teflon dielectric feeds the microwave radiation into a distorted coaxial structure which has a rectangular outer conductor and wide, paddle-like center conductor hereafter referred to as the septum. This shape was chosen to provide a reasonably large region with a uniform magnetic field into which the sample can be inserted.

The typical dimensions of the detwinned YBCO crystals suitable for microwave measurements have ab-plane area $\sim 1mm^2$, and c-axis thickness $< 50\mu$m. This is a consequence of the natural preference for the crystal growth which will be explained in section 2.7. The measurement geometry of this experiment is one where the sample lies flat on a sapphire plate with the magnetic field parallel to the broad face of the slab. The result is that the screening currents induced by the field flow in the ab-plane, perpendicular to the direction of the applied field. In this manner one can selectively measure $R_{s(a)}$ or $R_{s(b)}$. A complication is that current is also driven across the edge of the slab, and hence any measurement of the ab-plane R_s contains a small additive contribution from $R_{s(c)}$. This fact has been successfully employed by Hosseini *et al.*[20] at 22 GHz as well as Harris[11] at 75 GHz to extract $R_{s(c)}$ by carefully measuring the change in loss after the crystal was cleaved into a number of needles. They have observed that $R_{s(c)} \simeq 200\ \mu\omega$ at 22 GHz with a possible factor of two uncertainty, and approximately follows frequency-squared scaling to 75 GHz. In the case of this broadband experiment, the contribution is small for very thin crystals it will be shown in chapter 4 that it is a reasonable approximation to ignore the $R_{s(c)}$ component when examining the ab-plane electrodynamics.

Due to reflections, standing waves, and frequency dependent attenuation in the coaxial line between the microwave source and the low temperature experiment stage, the resulting microwave field at the sample varies considerably as a function of frequency. If the frequency response of the superconductor's absorption is to be properly monitored, then an independent measure of the cavity power level is required. The simultaneous measurement of the losses in a metal sample positioned on the other side of the septum serves this purpose. A reference sample obeying the classical skin effect was chosen since the frequency dependence of the loss can be calculated from a measurement of the DC resistivity(see Eq. 1.10).

For both the metal and superconducting samples, the microwave power absorption

per unit area is equal to $\frac{1}{2}R_sJ_{so}^2$ as given by Eq. 1.18. When placed in the same magnetic field, two conducting samples having the same dimensions experience the same induced surface current. Hence the ratio of superconductor to metal power absorption in the same field is seen to equal the ratio of the surface resistance values,

$$\frac{P^{S/C}}{P^{metal}} = \frac{R_s^{S/C}}{R_s^{metal}}. \tag{2.1}$$

All that remains for the extraction of $\sigma_1(\omega)$ from $R_s(\omega)$ is a value for $\lambda(T)$ which can be obtained by other experimental techniques as alluded to in chapter 1.

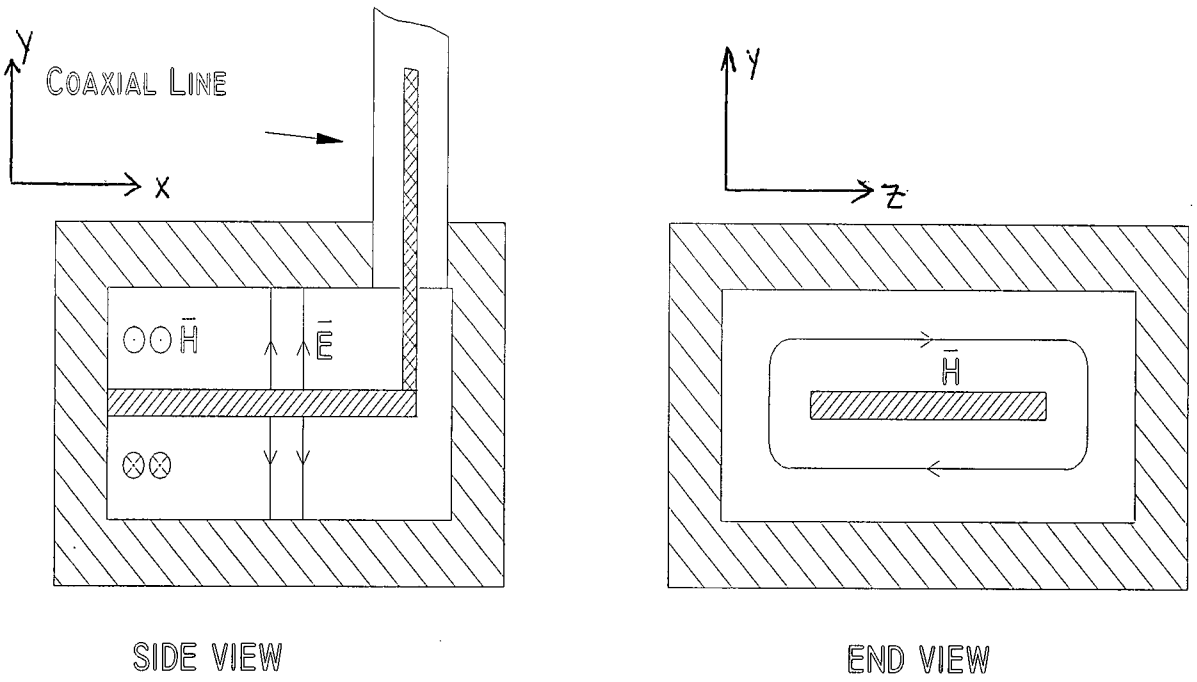

Figure 2.1: Schematic of field distribution in cavity. The sample is positioned in the region where H is maximally uniform and near the end wall where E is a minimum.

Fig. 2.1 depicts schematically the TEM field pattern for the terminated coaxial line. Initial work with this experiment revealed a number of undesirable resonances associated with waveguide modes in the cavity. These modes are clearly problematic since they can produce an asymmetry in the fields on the two sides of the septum which then affects the

sample and power meter sides differently. In order to extend the band of operation, the length of the septum region was shortened, effectively reducing the length of the cavity. Initially, the first resonance peak was at 18 GHz and the modification was successfully pushed it up to 22 GHz, which is now the limit of operation.

The apparatus has evolved as a modification of an existing penetration depth experiment, utilizing the same cryostat insert and sample holder.[21] The cavity is made of an assembly of copper pieces which bolts to the end of a standard design low temperature probe used by the UBC superconductivity group. A drawing of the cavity assembly with dimensions is shown in Fig. 2.2. This drawing only details the inside of the cavity where the microwave fields exist.

The construction of the cavity was a multi-stage process. The septum was cut from a .036" thick copper sheet and subsequently hard soldered into a groove which had been cut into a 1/8" thick copper plate. This endplate is what forms the termination end of the transmission line. At the other end of the septum, a solder joint is made to the centre conductor of the coaxial line. The endplate was then fitted into the copper body such that the septum was aligned as close to the centre of the cavity as possible. The entire inner assembly of the cavity, endplate and septum was heated above the melting point of soft solder and carefully tinned. This serves the dual purpose of mechanical support while providing a coating which becomes superconducting below about 7K. This superconducting coating drastically reduces the power absorbed by the cavity walls in supporting the RF currents associated with the fields. This is an important detail because modulated power absorption by the cavity structure can interfere with the temperature modulation of the sample stage. The 15 cm of coaxial line nearest to the cavity has also been carefully disassembled, tinned, and reassembled for the same reason.

The challenge of the accurate alignment of the septum while the solder was liquid proved to be difficult. This resulted in the septum being offset from the centre of the

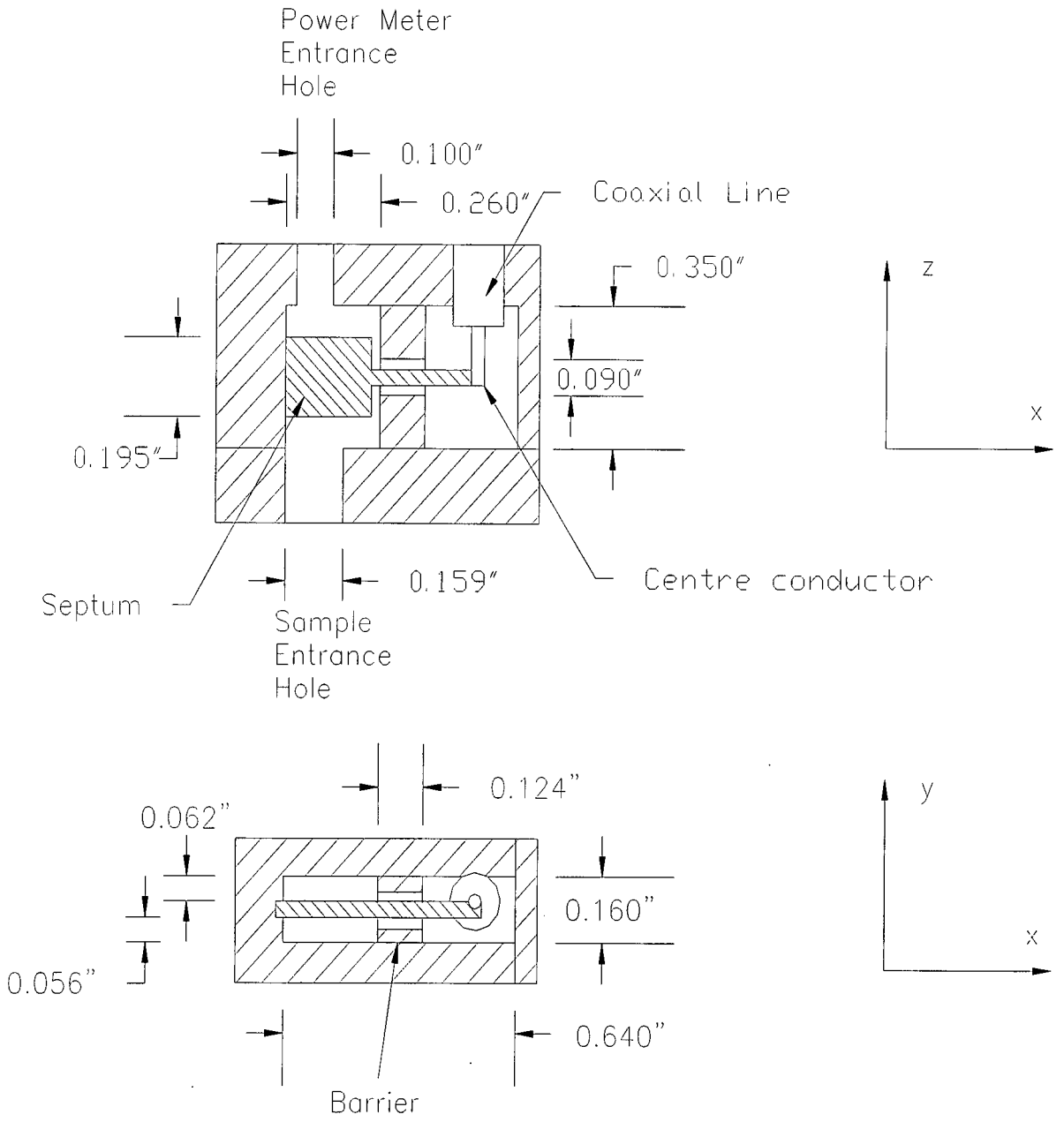

Figure 2.2: Schematic of cavity with dimensions showing the position of the septum and its offset from centre

cavity by 0.003". The asymmetry between the two sides means that the field intensities experienced by the sample and the power meter are different. This difference is measured during calibration and all experimental data must be correspondingly corrected.

2.2 The Sample Holder and Power Meter

One of the challenges with microwave spectroscopy is the unobtrusive suspension of conducting samples in a region of uniform magnetic field. A technique which was first described by Sridhar and Kennedy[22] and by Rubin *et al.*[23] is the use of a sapphire cold finger in vacuum. This method of placing superconducting samples in the magnetic fields of a variety of microwave resonators has been extensively used by the UBC microwave group[17]. The bolometry stage has been designed such that there will be a thermal mass which is isothermal with both the sample and thermometer. This isothermal stage is then weakly linked to the base temperature of the helium-4 bath which is held at 1.2K. The isothermal sage was designed using high thermal conductivity materials to avoid unwanted thermal gradients. The thermal penetration depth δ is a length scale characteristic of the distance that heat can diffuse in a time $2\pi/\omega$ where ω is the angular frequency of the oscillating heat source. δ is an intrinsic property of a material and is independent of geometry. The definition of δ is

$$\delta = \sqrt{\frac{K}{\omega}} = \sqrt{\frac{\kappa}{\rho C \omega}} \tag{2.2}$$

where $K = \kappa/\rho C$ is the thermal diffusivity, C is the specific heat per unit mass, ρ is the density, and κ is the thermal conductivity. The isothermal stage was designed using appropriate materials such that the thermal penetration depth δ would be much larger than any of the dimensions. The choice of material for the weak link was dictated by the requirement that δ be comparable to the dimension separating the isothermal stage from the bath. This permits the temperature oscillation of the sample, while ensuring

that the time constant for the stage to cool following power input is not too long. The thermometer is mounted on the isothermal stage, as well as a heater used for calibration purposes. Fig. 2.3 shows the details.

A copper base plate which is in good thermal contact with the temperature regulated helium bath provides the foundation for the sample stage. A sapphire disk epoxied to the base plate provides a platform onto which a thin walled quartz glass tube ($\ell = 1.2cm, O.D. = 5mm, t = 0.38$mm) is glued. The sapphire disk serves to sustain the differential thermal contraction between the metal and the glass, preventing the tube from being damaged. The other end of the quartz tube is terminated with a small sapphire block. A CX-1050 Cernox resistive thermometer from Lakeshore Cryotronics is fastened with G.E. varnish to the sapphire block to ensure good thermal contact. In a similar fashion, a chip resistor is mounted which acts as a heater. Extending from the sapphire block, parallel to the axis of the quartz tube, is a high purity sapphire plate ($0.1mm \times 18mm \times 0.6$mm). Great care was taken in fabricating the sapphire block to ensure that the sapphire plate, and hence the sample, lies parallel to the end wall in the cavity. A small sapphire offset spacer ($6mm \times 2.14mm \times 0.56$mm) between the sapphire block and plate proved necessary to properly position the sample due to the fact that this experiment is a retro-fit to an existing probe. The sapphire plate is held to the sapphire block by means of a small amount of DuPont silicone vacuum grease. A non permanent adhesive is desirable since it permits the removal of the plate for cleaning, as well as minimizing the chance of breakage during sample mounting. The result is a rigid stage at cryogenic temperatures which permits very little movement of the sample in the fields. The combination of sapphire along with the heater and thermometer comprise the isothermal stage of the design, while the quartz glass tube acts as the thermal weak link.

The sapphire plate extends through a hole ($\phi = 4.03$mm) in the cavity with the tip arranged to be at a location with uniform H. This hole diameter is chosen to be beyond

cutoff for the microwave frequency range encountered, and also does not significantly distort the field profile. The sample is mounted on the end of the sapphire plate with a very small amount of silicone grease. This provides adhesion as well as the necessary thermal contact. Sapphire is chosen for the cold finger because it is available commercially with very high purity levels.[1] This sapphire exhibits a very low loss tangent[24], low magnetic susceptibility, and high thermal conductivity at low T ($\kappa = 5 \times 10^{-2} \frac{W}{cmK} @ 1K$). Recent unpublished dielectric measurements at UBC have confirmed the low loss tangent in sapphire. The high thermal conductivity of the sapphire plate and block ensure that the thermometer reflects the temperature of the sample. Fig. 2.3 depicts the sapphire cold finger assembly in detail.

It is useful to note for design purposes that experimental data on the low temperature specific heat and thermal conductivity for quartz glass (vitreous silica) can be found in Refs. [25] and [26]. Similar data for synthetic sapphire (Al_2O_3) can be found in Refs. [27] and [28].

It has been established with experience that great care must be taken to clean any sapphire which is subjected to electric fields in order to keep dielectric losses low. Any time that contamination is expected, a special procedure for cleaning the sapphire using a series of increasingly low residue solvents is performed. This has become routine in the UBC superconductivity lab using a recipe which was originally obtained from the Jet Propulsion Laboratory, NASA, and is included in Appendix 2. On a more regular basis (*i.e.* between runs) grease at the sample tip is removed with a swab of low lint tissue and trichloroethylene as a solvent.

Four electrical leads are required to make a four wire measurement of the Cernox resistance, while another two leads inject the current into the heater. These wires are

[1] Plates are cut from Saphikon Brand high purity sapphire disks. Purity=99.997% with the dominant impurities (PPM) being Fe(2), Mo(4), Si(15), Mg(2), S(3), Ca(1), Cr(0.3).

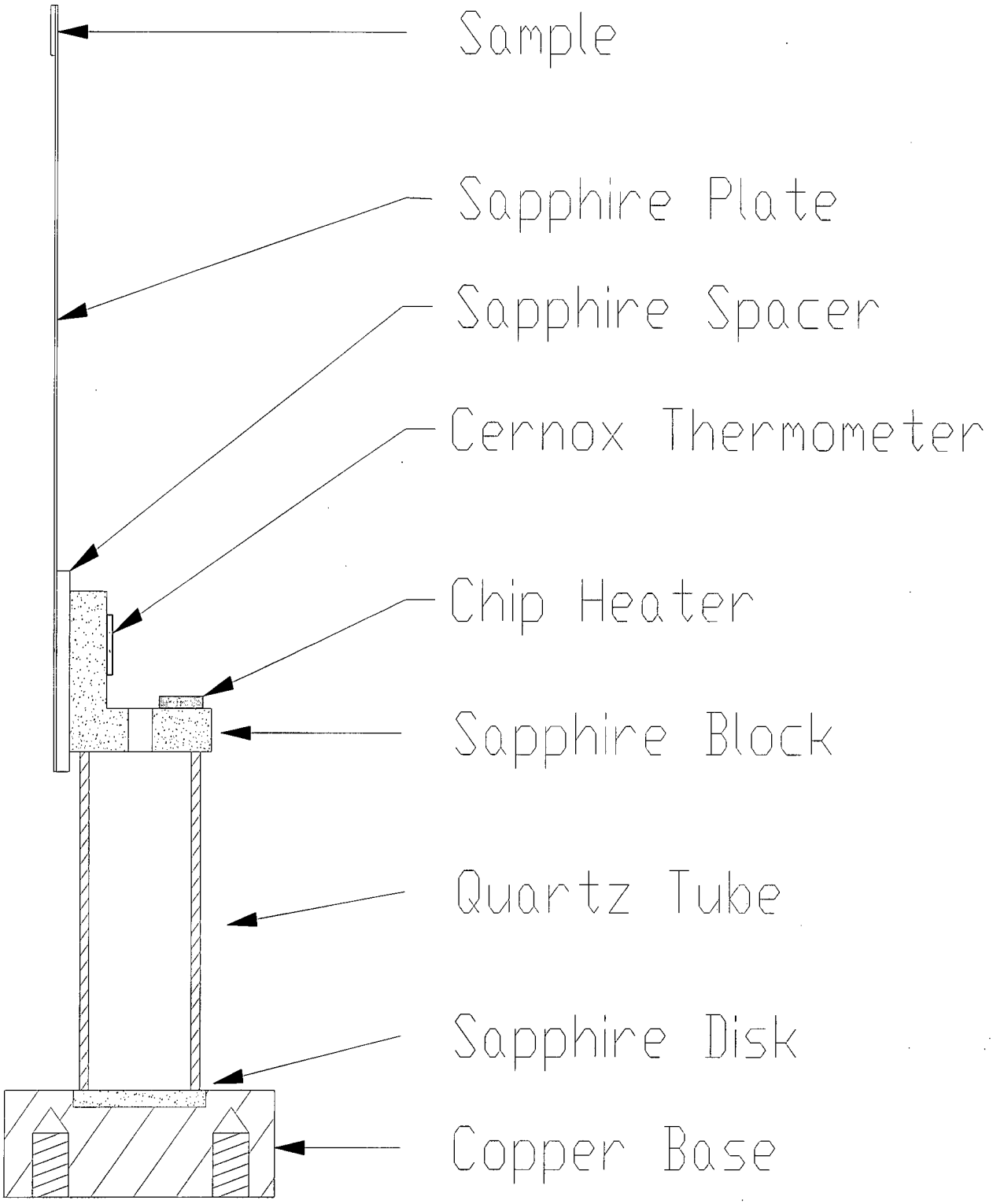

Figure 2.3: Details of the quartz and sapphire sample holder. The quartz tube has dimensions $\ell = 1.2cm, O.D. = 5mm, t = 0.38$mm.

very fine brass (No.40 AWG) which minimizes the thermal conduction parallel to the quartz tube. After extending down the length of the quartz tube and being sufficiently heat sunk to the base, a transition to more robust wires is made. These wires enter the vacuum can via holes drilled through the bottom of the copper pot and the holes are sealed with Emerson and Cummings brand Stycast 2850-FT epoxy. This epoxy is highly filled with sapphire powder which serves to reduce the thermal expansion to a near match with brass. The result is a robust hermetic feedthrough, which will not be damaged by thermal cycling.

In order to account for the frequency variation of the microwave power reaching the cavity (as described in section 2.1), a second sample holder was installed to function as a power meter. The power meter supports a sample of reference material which has a known microwave loss, and permits the calculation of the value of $R_s(\omega)$ for the unknown material on the sample side according to 2.1. The principle of design is the same as the sample side, however different construction materials were used. The quartz tube used on the sample stage was replaced by a thin walled stainless steel tube ($\ell = 3.5mm, O.D. = 1.6mm, t = 0.3$mm), and the sapphire block replaced by a copper block. Due to the fact that the microwave power absorption of a metal is roughly three orders of magnitude larger than YBCO, the same degree of sensitivity is not required. Thus the task of working with sapphire and quartz was avoided and metallic construction materials were chosen because they are easy to work with. The copper has a very high thermal conductivity, and is thus suitable for thermometry and sample mounting, while the stainless steel has a significantly lower conductivity and is suitable for the thermal weak link to the bath. The details of the power meter assembly are shown in Fig. 2.4.

The copper manifold which accommodates the power meter is bolted to the microwave cavity from above. The power meter itself is held into this manifold by means of two set-screws. Another set-screw secures the copper and epoxy plug which houses the electrical

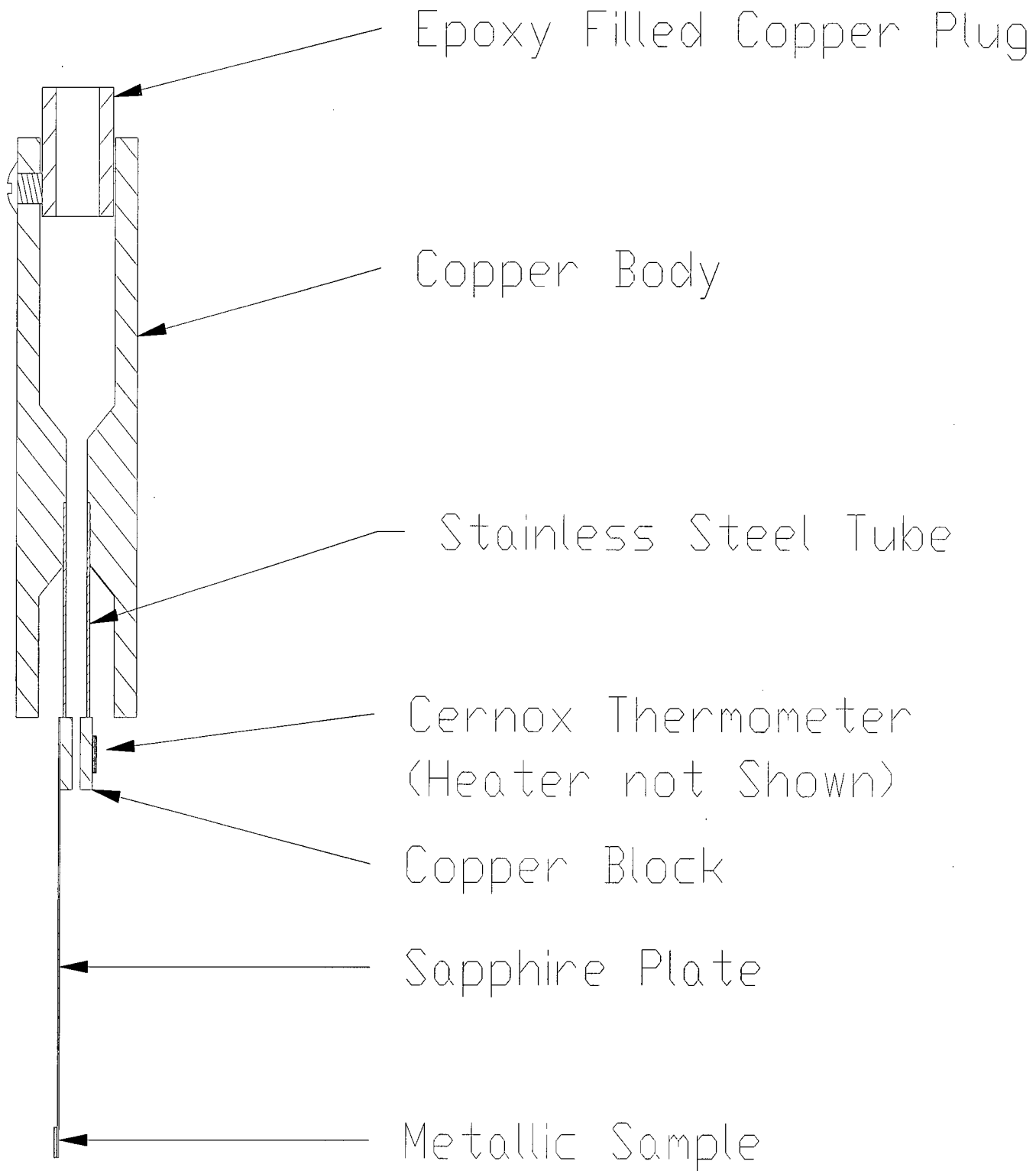

Figure 2.4: Details of the stainless steel and copper power meter. The stainless steel tube has dimensions $\ell = 3.5mm, O.D. = 1.6mm, t = 0.3$mm.

leads to the upper end of the power meter assembly. It was realized that the direct thermal contact between the power meter and the cavity poses problems with microwave power being dumped into the cavity thus reaching the power meter as stray thermal signal. In order to prevent this, the power meter was lifted off of the cavity block by means of three pieces cut from a nylon washer. This was done in an attempt to introduce a thermal time constant which is much greater than the oscillation period of the modulated microwave power. The estimated time constant of the nylon spacers and bolts is 17s, which would serve to suppress 1/2Hz oscillations by a factor of about 25. Upon cooling to 1.2K, it was discovered that the thermal link to the bath was not good enough to dump the heat leaking from the brass electrical leads descending from room temperature and the power meter did not cool below about 4K. To improve this link, eight copper wires (No.22 AWG) were installed running from the power meter base to the inside of the vacuum can. These wires are clamped to the base with more copper wires, and wedged against the inside of the brass vacuum can by a smaller diameter copper ring. Both ends of the wires were hammered flat to increase their surface area, and covered in G.E. varnish to improve thermal contact.

Six brass wires (No.32 AWG) run down the centre of the cryostat, providing the electrical contact to the Cernox 1050 thermometer (four leads) and chip heater (two leads). To facilitate disassembly, they are connected to micro jack connectors at the other end which join to shielded stainless steel wires that travel the length of the cryostat up to a hermetic feedthrough. Similar to the sample side, the sapphire plate which suspends the sample in the magnetic field is mounted on the copper block with silicon grease and a small amount of G.E. varnish for security. The metallic sample is mounted on the sapphire plate with a very tiny amount of silicon grease, as is the superconducting sample.

The entire probe assembly is depicted in Fig. 2.5. Some items including the electrical

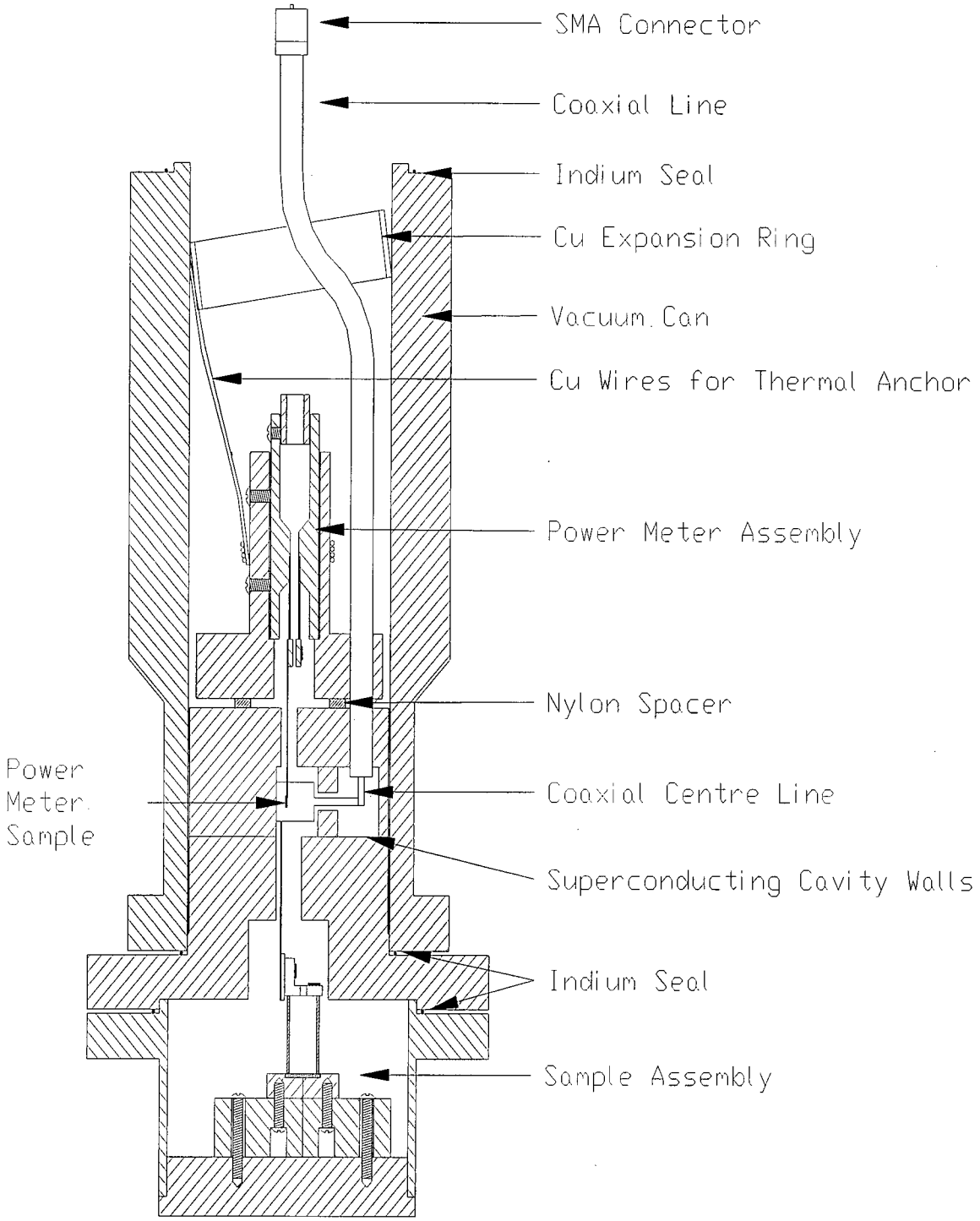

Figure 2.5: The entire probe assembly.

leads to the various thermometers and heaters, and many of the bolts which are used in the assembly of the cavity are omitted for simplicity. The superconducting sample is not visible in this drawing since it is on the far side of the septum.

2.3 Low Temperature Thermometry

The experimental assembly is housed at the end of a 4' long cryostat insert which positions the cavity assembly near the bottom of a glass liquid helium dewar. The insert, which accommodates the coaxial line, electrical leads, sample stage, power meter, and cavity, is evacuated to high vacuum before cooling is commenced. Upon cooling of the cryostat to liquid nitrogen temperature, liquid helium is transferred into the surrounding dewar. Cooling below the helium boiling point of 4.2K is achieved by means of a high throughput Stokes pump which reduces the vapor pressure and hence the temperature of the helium bath. The lowest temperature attainable with this arrangement is just under 1.2K (corresponding to a vapour pressure of roughly 0.3 Torr). This temperature is well below the superfluid transition temperature of helium, which means the bath will not sustain temperature gradients due to an exceedingly high thermal conductivity.

An Allan Bradley carbon composition resistor mounted on the outside of the probe acts as a bath thermometer. In the 1 K temperature range, it has a sensitivity near 5 $k\Omega/K$. This thermometer in conjunction with a carbon glass resistor acting as an ohmic heater and a UBC made temperature controller (model 85-003) permits bath regulation stable to less than a fraction of a mK. Bath regulation is important since it maintains constant temperature over the duration of an experiment which can exceed 6 hours. In addition to compensating for the varying microwave power which is dumped into the bath, the regulation also prevents the slow reduction in temperature as the volume of helium in the dewar is reduced and the pumping efficiency increases.

As will be discussed in the next section, the overall sensitivity of the bolometric measurement technique employed by this experiment is greatly influenced by the choice of thermometer. In addition to very high temperature sensitivity (*i.e.* dR/dT), the thermometer must have a negligible heat capacity compared to the rest of the sample stage. Lakeshore Cryotronics produces a series of sapphire mounted oxide film thermometers which meet these requirements. Two Cernox 1050 model thermometers were specially ordered, chosen to have large dR/dT values at liquid helium temperatures. The resistance of these thermometers increases by three orders of magnitude in going from room temperature to 1K, with a very dramatic increase below 4K. Near 1.2K the sensitivity exceeds $100k\Omega/K$.

The two thermometers mounted on the sample and power meter were calibrated against the vapour pressure of liquid helium 4 (using the 1958 Helium Temperature scale)[29]. In order to avoid complications with pumping gradients, the calibration was performed with enough helium gas admitted to the vacuum chamber that liquid was present. The helium bath was pressure regulated to achieve constant temperatures over the range of interest while the helium vapour pressure inside the probe was monitored to infer the calibration temperature. Four wire measurement of the resistance thermometers were made using UBC made automatic resistance bridges (model 83-047). The bridges employ a 30Hz AC measurement technique which was verified not to dissipate significant power in the resistors. Slight variations between calibrations and uncertainty in pressure readings put an overall uncertainty in absolute temperature at $\pm 20mK$. Fig. 2.6 displays the low temperature calibration for the Cernox 1050 thermometer used on the sample stage. The resistance increases rapidly over the range of 3.5-1.2K which makes it an ideal thermometer at these temperatures. A power law fit to the calibration data is used during an experiment to infer the temperature of the sample.

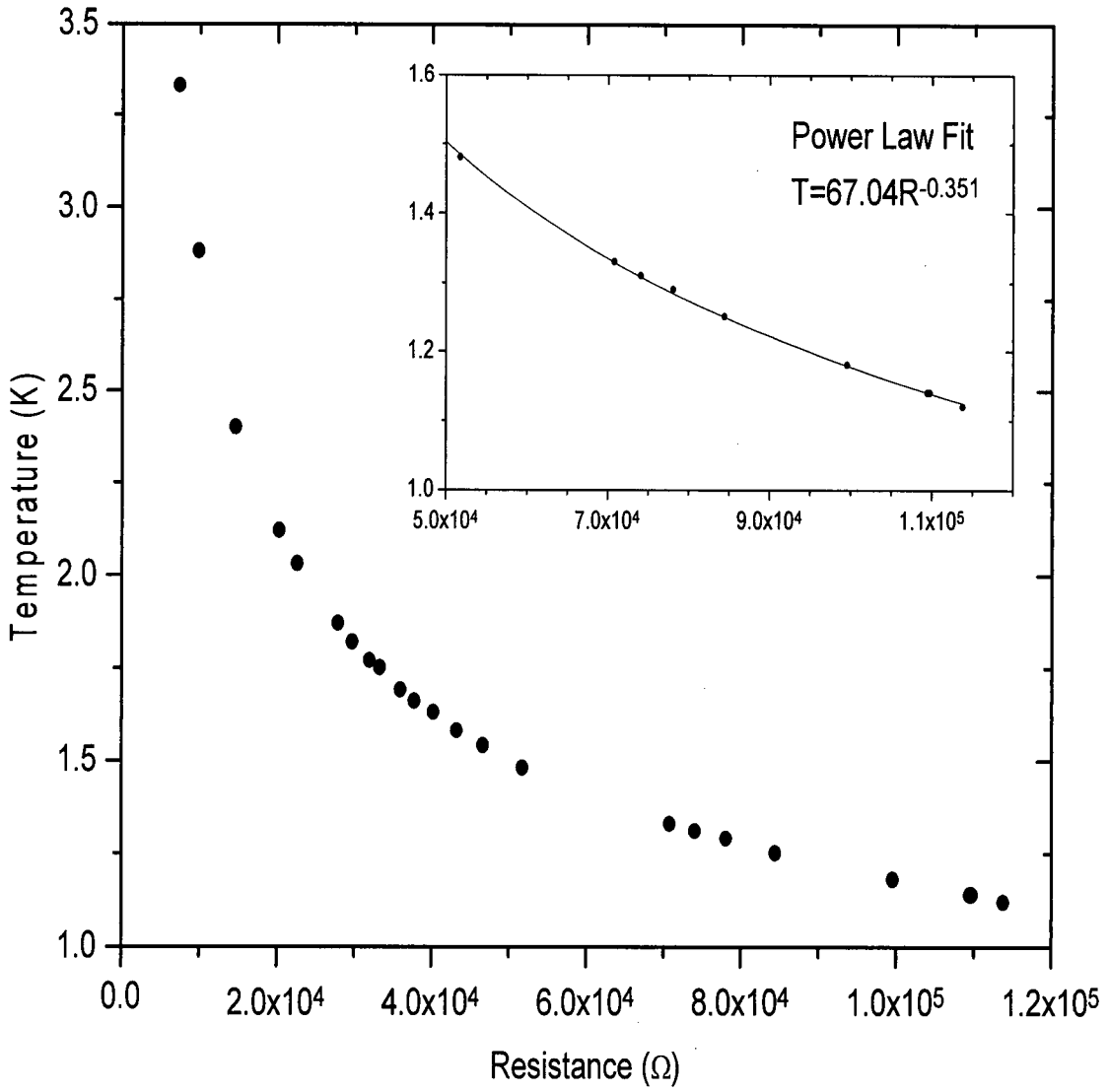

Figure 2.6: The low temperature calibration of a Cernox 1050 resistance thermometer from Lakeshore Cryotronics. The power law fit shown in the inset is very good in the low temperature range.

2.4 Modulation and Reference Signal

The phase-sensitive measurement technique used in this experiment requires a reference signal to modulate the microwave power and to reference the lock-in amplifiers. The choice of frequency at which to operate requires careful consideration. The first factor to consider is the frequency dependence of the thermal response of the sample and the power meter stages (this data will be presented in chapter 3). The thermal response is attenuated as the modulation frequency is increased, and there is a roll off which depends on the thermal time constants of the elements of the stage. The measured data reveals that beyond a frequency of 1/2 Hz the thermal response of the sample stage begins to decrease rapidly. The second factor is the noise sources which are present in the system. Natural noise sources almost always have a 1/f spectrum, motivating the move to higher frequency modulation. Following testing of the signal to noise ratio with different modulation frequency, the decision was made to maximize the thermal sensitivity of the probe and use the low frequency 0.45 Hz modulation. The odd choice of 0.45 Hz rather than 1/2 Hz was due to the maximum speed of an older computer which was used to produce the sinusoidal modulation signal via a digital to analog converter.

A 486 PC equipped with a two channel digital to analog converter is used to simultaneously produce the power modulation signal as well as the reference signal for the lock-ins. The modulation signal is fed to the HP 83630A synthesized sweeper AM MODULATION input. The instrument is set internally to scale the output power 100%/V such that the output is scaled linearly with the input which is between -1 and 0V. The modulation signal which is used varies in time as

$$v(t) = \sqrt{\frac{1+\sin(\omega t)}{2}} - 1. \tag{2.3}$$

This is done such that the power dissipated in the samples will only contain a component

at frequency ω since power is proportional to v^2, *i.e.*

$$P(t) = P_o\left(\frac{1+\sin(\omega t)}{2}\right). \tag{2.4}$$

If the response of the system is linear, then there is no concern with other harmonics being present in the signal. The use of this modulation signal simply ensures that the maximum possible microwave power is present at frequency ω. The other channel of the digital to analog converter is used to produce a sinewave of frequency ω with an amplitude of $2V_{pp}$. This is necessary because below 1 Hz the lock-in amplifiers prefer sinewave reference signals.

2.5 Detection Circuitry

The experimental quantity of interest is the thermal response of the superconducting sample. At low microwave frequency R_s becomes barely discernable from the noise in the system, and it becomes important to optimize the measurement technique. The resistance of the Cernox thermometer R_C indicates the temperature of the sample. This resistance value is monitored by measuring the potential drop when biased with a constant DC current. The voltage signal V is multiplied sequentially by two instrumentation amplifiers before reaching the lock-in amplifier. Since the voltage signals of interest are very low level, signal conditioning must be done carefully. The voltage signal is brought via shielded wires from 1K up to the electronics which are housed outside of the cryostat at room temperature. The signal is brought into a closed steel box which acts as a shield from stray electromagnetic radiation where the amplification electronics are housed. All leads which run between the cryostat and this "bias box" are shielded with copper braid to reduce pick-up and are of the shortest length possible. The amplifiers serve to increase the magnitude of the voltage signal, as well as to provide buffered outputs which alleviates

concern about external noise getting back into the circuit when making connections to other instruments. Fig. 2.7 shows the bias circuit and the voltage monitor.

The constant current source which provides the bias current to the Cernox consists of a 1.5V alkaline battery in series with a resistor whose value is much greater than that of the Cernox. The alkaline battery provides a very quiet voltage source and does not require external connections to circuits which may introduce ground loops. The voltage drop across the Cernox is expressed as

$$V = IR_c = V_c + v_c. \tag{2.5}$$

where the DC voltage V_c indicates the temperature of the sample stage while the AC response v_C corresponds to the oscillations due to the microwave heating providing a total signal which is the sum of the two. Upon entering the bias box, the signal is brought to an Analog Devices AD620 low noise instrumentation amplifier. The gain of this amplifier has been measured to be 10.04. In the spirit of keeping the system noise at a minimum, all of the active components in the bias box are powered from 12 V batteries. Following this gain V_c is measured after passing through an AD548 Op Amp acting as a follower to buffer the output. Since V_c is typically of the order of 100 mV, the gain of 10 provides a signal which is convenient for measurement. Between the first amplification stage and the second is a 15 Hz low pass filter which removes high frequency noise. In order to prevent saturation of the second stage of the amplifier circuit, the DC offset is subtracted at the input to the AD548 amplifier by summing it with a variable DC voltage. A second AD548 amplifier with a gain of 9808 is the final element in the circuit. The overall gain of 10^4 puts the AC signal v_c in the range of hundreds of mV, a suitable range for the lock-in amplifier. The output of the bias box is equipped with a Burr Brown ISO122 capacitively coupled isolation amplifier which prevents the introduction of ground loops to the circuit.

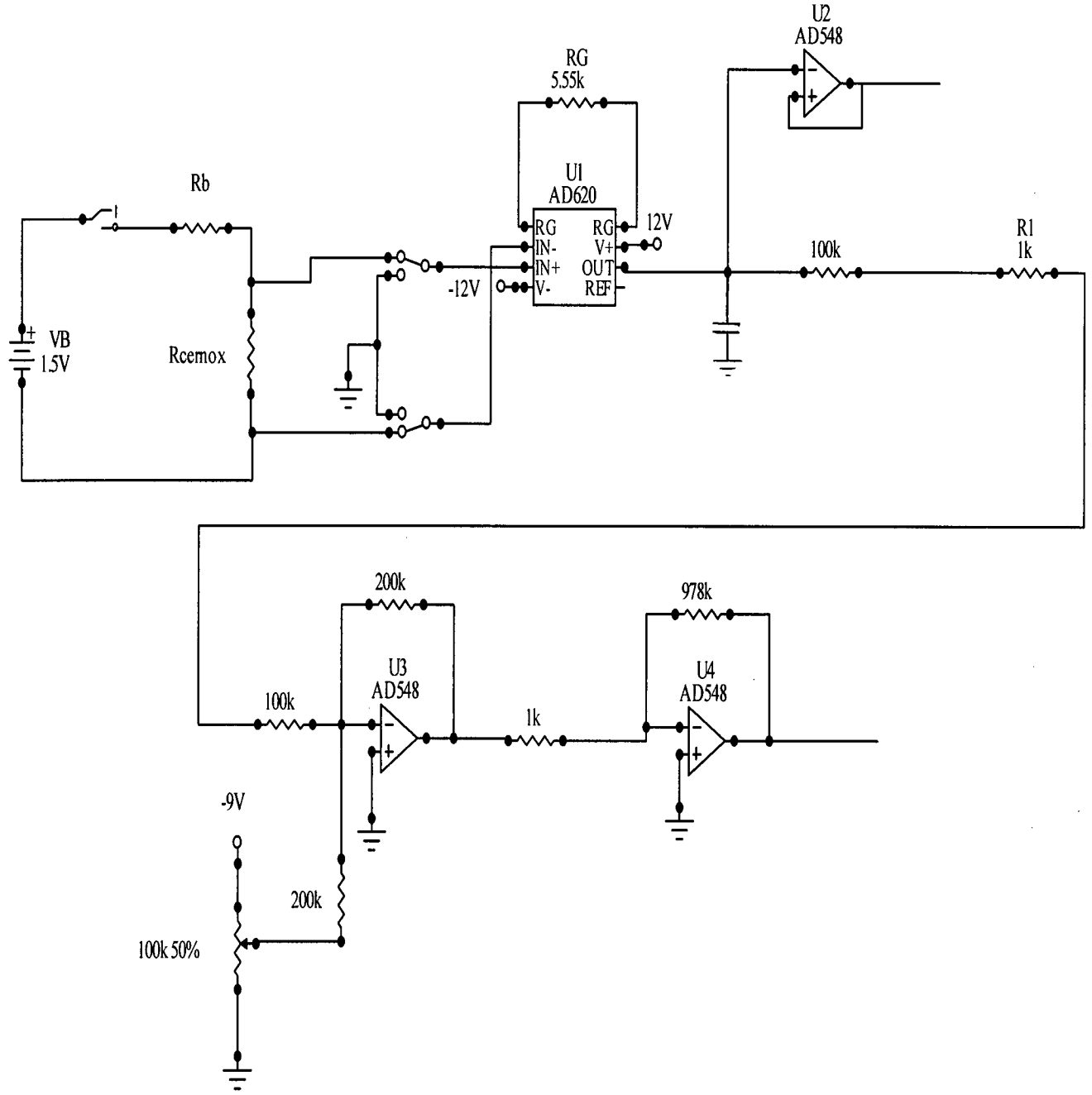

Figure 2.7: Bias and amplification circuit for sample thermometer. Gain of U1 is 10, U2 is unity, U3 is summing, and U4 is 10^3. The output of U2 is to monitor the DC voltage across Rcernox, and the output of U4 is fed through an ISO122 isolation amplifier and on to the SR850 lock-in amplifier.

In order that the maximum sensitivity be obtained, the bias conditions must be chosen carefully. If the Cernox resistor is biased with a current I_{bias} at a temperature T, and the heat flux into the stage arising from the microwave absorption of the sample is $\dot{Q}$ then the time varying voltage induced across the Cernox is

$$v_c = I_{bias} \frac{dR}{dT} \frac{\dot{Q}}{K} \tag{2.6}$$

where K is the effective thermal conductivity of the stage. From this expression it is clear that the sensitivity of the response to power input is proportional to both dR/dT and I_{bias}. Unfortunately these two quantities are not independent since dR/dT of the Cernox drops rapidly with increasing T and increasing I_{bias} increases the temperature of the stage. The optimal signal to noise is obtained when I_{bias} is brought up to a level where the Cernox just begins to self heat due to the competition between the two effects. This is the reason that data has been taken at 1.3 K rather than the bath temperature of 1.2 K. It turns out that the signal to noise ratio is reduced but still reasonable if I_{bias} is increased enough that the sample warms to 1.8 K, and some preliminary 1.8 K data has been collected.

There are two main sources of noise which affect this experiment. The first is electronic noise, including Johnson noise and shot noise arising in the passive and active elements in the detection circuit. The second is that of the temperature fluctuations of the helium bath. It has been found experimentally that the dominant noise source is that of the bath temperature fluctuations which are inherent to this type of helium cryostat.

On the power meter side, the losses in the metallic sample are greater and thus for a given microwave power level the thermal response will be much larger than for a YBCO sample. Hence the same degree of high gain, low noise circuitry is not required for the power meter. The UBC made automatic resistance bridge described earlier is used to monitor the resistance of the reference Cernox. The bridge has the capability

of providing an error signal voltage which is proportional to the difference between the resistance reading and a reference value. This error signal is fed to a lock-in amplifier providing a means of monitoring the temperature oscillation of the power meter stage.

Following the insertion of the nylon spacers and copper wires for thermal anchoring, it was observed that the DC temperature of the stage varied according to the microwave power level in the cavity. The thermal anchoring of the power meter stage to the bath was not sufficient to prevent the warming of the stage with increased power input. This introduced the unfortunate situation whereby the sensitivity of the bolometer (which is highly temperature dependent) would vary with microwave power level. Since the microwave power reaching the cavity is frequency dependent, the sensitivity variation was a serious concern.

To get around the sensitivity variation, the DC temperature of the reference stage is regulated using the chip heater which is mounted on the copper block. A reference value is set on the resistance bridge which puts the temperature of the stage above the highest temperature that the microwave power will induce. A UBC made temperature controller (model 85 003) is used to maintain the set temperature value. In order to remove the AC component from the error signal emerging from the bridge, a low pass filter is employed. It is important that the filter remove effectively all of the signal at the modulation frequency ω because if the temperature controller were responding at ω it would interfere with the true signal.

The filter chosen for this task is a second order Butterworth filter. The merit of the Butterworth filter is an optimally flat passband at the expense of a somewhat less steep transition region. For further details, the reader is directed to the very useful book of Horowitz and Hill [30]. As required, the two RC pairs are matched in the two stages of the circuit with values of $R = 396.4k\Omega$, $R' = 232.3k\Omega$, and $C = 1.487\mu F$. The measured transfer function is shown in Fig. 2.8, and it is seen that $f_c = 0.035Hz$ and the

attenuation relative to DC at $0.45Hz$ is -24 dB. The small gain of roughly 2dB in the passband of the filter does not pose any problems, it simply means that the regulation temperature is slightly above the set point temperature on the resistance bridge.

2.6 Instrumentation and Software

Fig. 2.9 provides a block diagram of the electronics which are utilized by this experiment. At the heart of the operation is a 166 MHz Pentium PC which performs data acquisition and instrument control via GPIB. The PC controls the power level and frequency of the HP 83630A synthesized sweeper (0.01-26 GHz) as well as the operation of two Stanford Research Systems Model SR850 DSP lock-in amplifiers which perform the data collection. To increase the power incident on the septum, a microwave amplifier follows the synthesized sweeper. Depending on the frequency range, either the HP 8349B (2-20 GHz) or the HP 8347A (.01-5 GHz) is used. A second PC which contains a dual channel Eagle Technologies PC74 brand digital to analog converter provides the signal required for the modulation of the microwave power and the signal to reference the lock-in amplifiers.

During the collection of data, the only connection to the sample stage are the leads which monitor the Cernox voltage. On the power meter side, both the Cernox thermometer and the chip heater are required since the DC temperature of the stage is to be regulated. The reference value of the resistance bridge is set such that when the error signal passing out the back of the bridge is nulled, the stage rests at the desired temperature. The error signal is filtered with the low pass filter to remove the AC component and fed to the temperature controller which can dump power into the chip heater to regulate the temperature.

Both the sample and the power meter voltage signals are passed to the CH1 inputs of

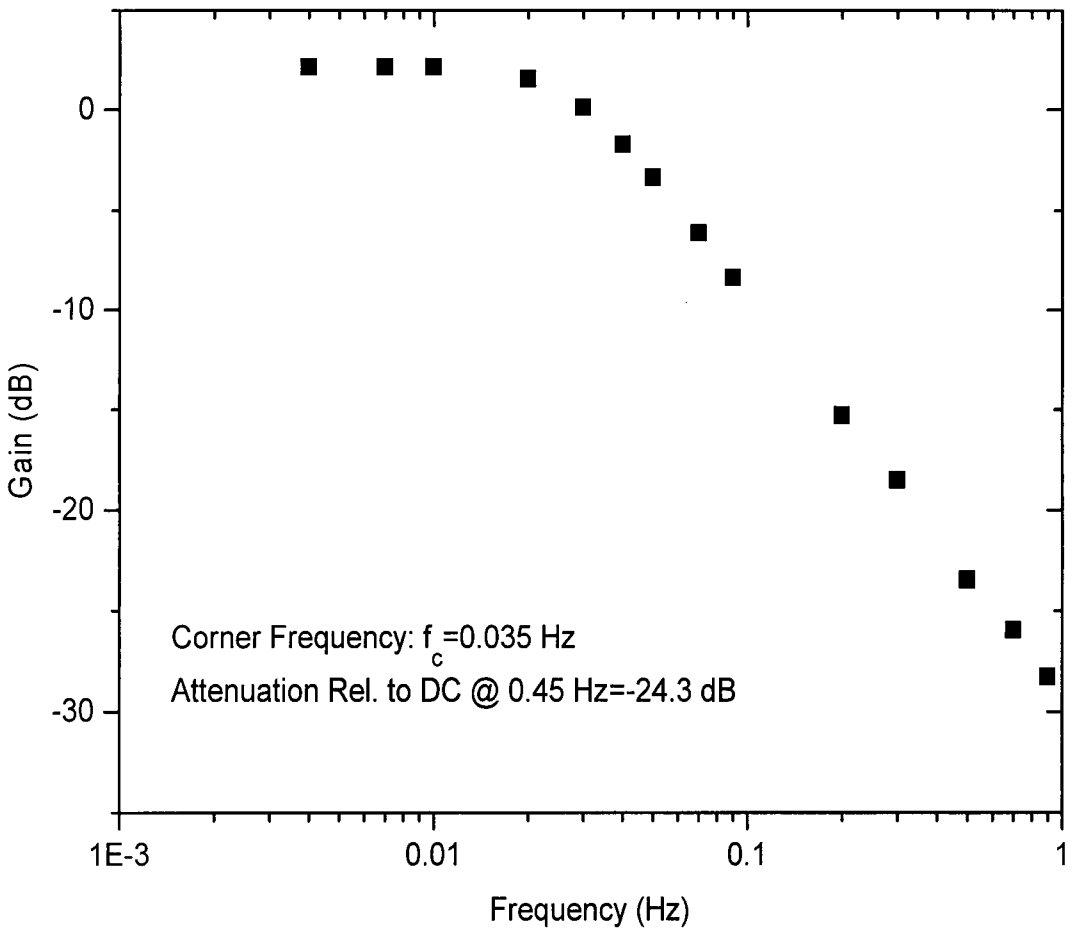

Figure 2.8: Measured transfer function of second order Butterworth filter. The microwave modulation frequency of 0.45Hz is strongly attenuated by this filter, ensuring that the feedback operated temperature controller does not contribute to the experimental signal.

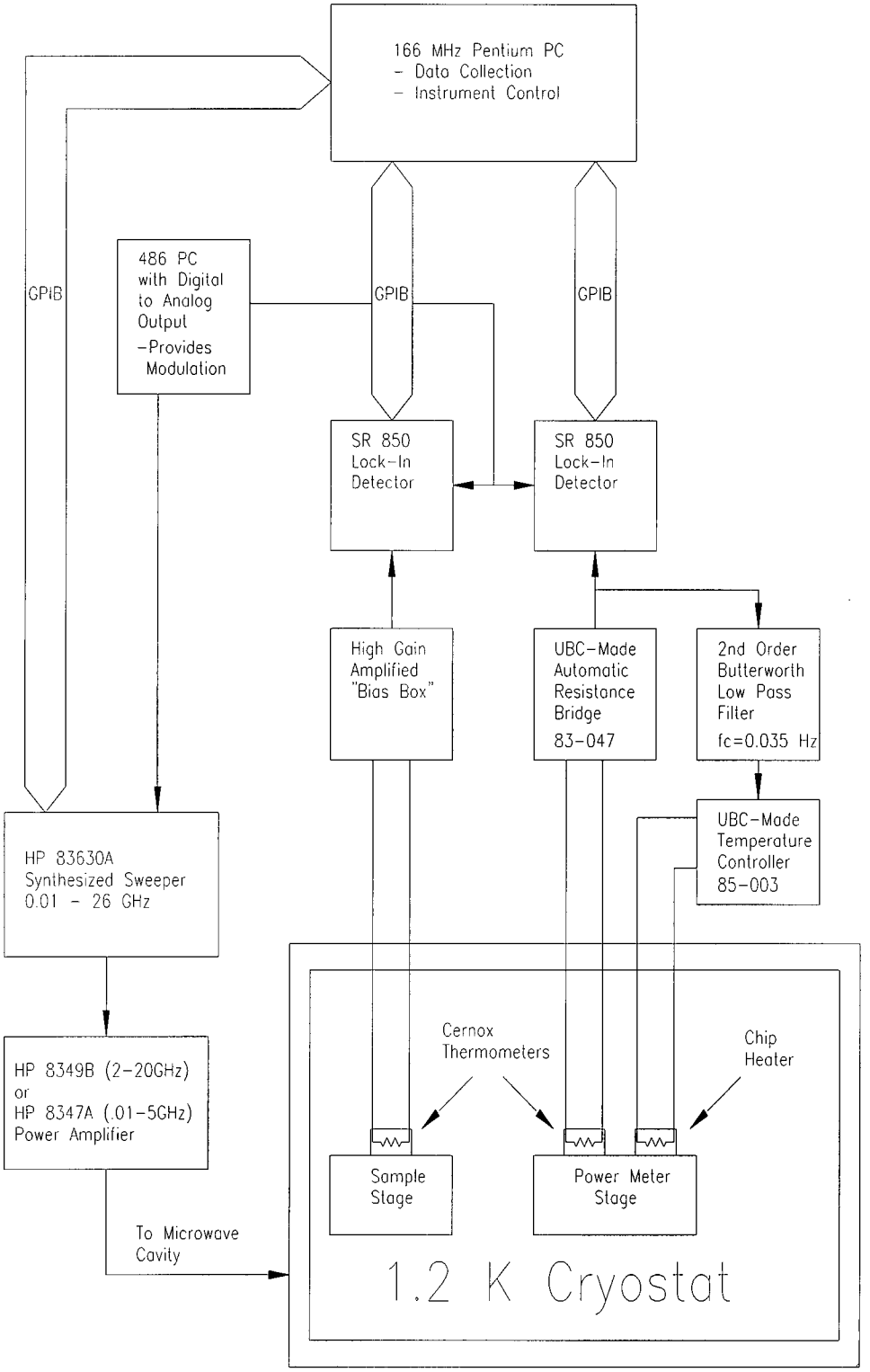

Figure 2.9: Electronics Block Diagram.

two SR850 lock-in amplifiers. At a fixed microwave frequency and power level, the lock-ins trace the input over a 60s scan. Following the scan, the average value of the in phase response X and out of phase response Y are transferred to the PC. The PC then calculates the average value of the magnitude of the response, $R_{avg} = \sqrt{X_{avg}^2 + Y_{avg}^2}$. The use of the computer is necessary because the algorithm used by the SR850 to calculate R does so in a fashion which does not average X and Y, but rather calculates R instantaneously. The result of this is that the noise does not average to zero over time.

Once the experiment has been cooled and fully calibrated, the control of the experiment is handed over to the PC. A program has been written in Microsoft's Visual Basic programming language which completely automates a frequency sweep. Any number of discrete frequency data points can be taken over the range .01-20 GHz. The program monitors the magnitude of the signal on the sample side, and adjusts the power level at each frequency to maintain a nominally flat response. This avoids any signatures in the data that could be associated with the variation in sensitivity as it is known that drastic variations in microwave power level will alter the DC temperature of the stage and hence the sensitivity. Typically two data points are taken at each frequency at 200MHz intervals across the spectrum over the course of about 6 hours. Having two data points provides a measure of the noise on the data while not excessively increasing the amount of time required for a sweep.

2.7 YBCO Single Crystals

$YBa_2Cu_3O_{7-\delta}$ (YBCO) remains the most widely studied of the oxide superconductors for a number of reasons. It has a well defined ion stoichiometry which helps to ensure homogeneity, a variable and well defined oxygen content, and large single crystals are relatively easy to grow.[31] Many groups have worked with both single crystals and thin

films of YBCO since it was discovered in 1987 and much literature exists on the subject. Due to the complexity of these materials, the progression of the field has been limited by the understanding of how to control their properties. Measurements of the intrinsic properties have often been complicated by sample to sample variations in chemical purity and crystalline perfection. It has become clear that very good control over the materials is an absolutely critical component of any HTSC research.

Single crystals of YBCO have been successfully grown by a self flux method for some time now by Dr. Ruixing Liang at UBC.[32] With this method, the parent compounds are heated to about $1000^{o}C$ in a crucible which contains the $Y_2O_3 - BaO - CuO$ melt. As the melt is cooled, a temperature gradient causes the crystals to nucleate out of the melt onto the crucible walls. The growth rate of YBCO is most rapid along the ab-plane, and the largest crystals tend to grow with the $\hat{c}$ axis parallel to the crucible wall, extending outward from the crucible. They have sizes of up to several mm in the ab-plane and less than 1mm in the $\hat{c}$ direction. Following growth the crystals are detwinned under uniaxial stress at elevated temperature. Subsequently the oxygen content is set with a carefully controlled oxygen anneal.

The YBCO melt is highly corrosive, and attacks the crucible which contains it. Contamination from the crucibles has been a major source of impurities in the resulting crystals and hence much work has gone into exploring different options for crucible materials. Until recently, most crystals grown for the study of intrinsic properties have been grown using YSZ (Y_2O_3 stabilized ZrO_2) crucibles resulting in YBCO crystals which are limited to about 99.9% purity.

Recently there has been a remarkable improvement in the growth of single crystals of YBCO. The accomplishment which made this possible was the development of $BaZrO_3$ crucibles which are inert to the high temperature melt.[33, 34, 31] The result has given the UBC superconductivity group the ability to produce and study YBCO crystals which

display a factor of 20 increase in purity (99.99-99.995%). These crystals also have extremely narrow X-ray rocking curves, and very weak magnetic flux pinning both of which indicate a never before seen degree of crystalline perfection.[31] These next generation crystals have since been passed on to a number of experiments, and much current research focuses on these crystals which should provide a clearer pathway to a determination of the intrinsic properties.

The increase in crystal quality presented unexpected problems with regard to oxygen homogeneity along the copper oxygen chains, since the mobility is much less hindered by defects in the crystal lattice.[31, 35] For the work in this thesis we have worked with oxygen overdoped crystals ($O_{6.993}$) which do not show signs of oxygen clustering. While these crystals do not have the optimal T_c value, was important that oxygen inhomogeneities did not contribute to the observed behaviour by providing scattering centres.

Figure 2.10 presents the cavity perturbation results of Hosseini *et al.*[8] on a single $BaZrO_3$-grown crystal. The data is plotted as R_s/f^2 to account for the frequency-squared dependence from superfluid screening. It reveals very weak impurity scattering and the associated long quasiparticle lifetimes, verifying the improvement over the YSZ-grown crystals. From this data, the temperature dependence of the microwave conductivity spectrum from 1-75 GHz has been extracted, and this data will be compared to the bolometric data in chapter 4.

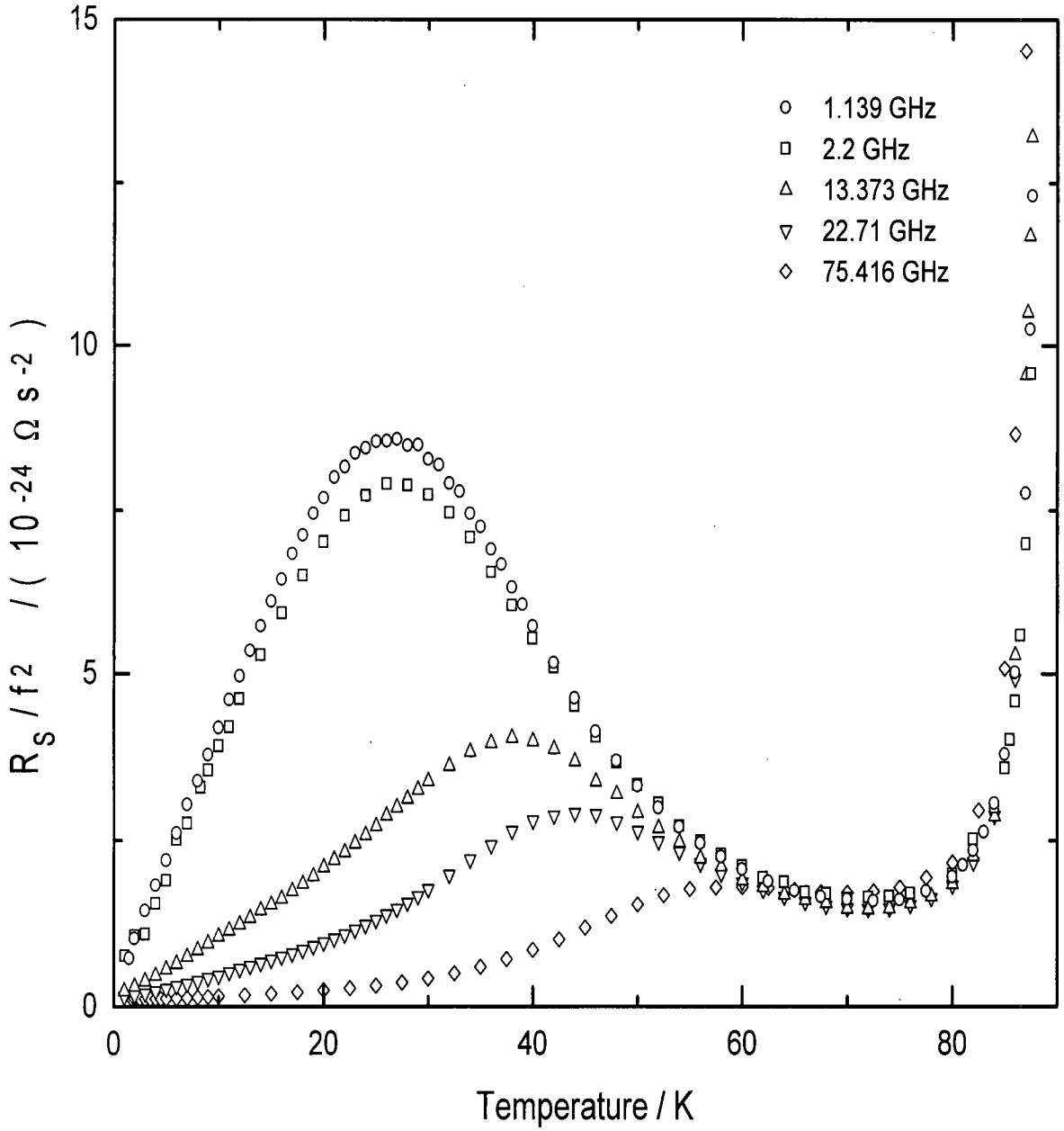

Figure 2.10: Cavity perturbation measurements by Hosseini *et al.* of $R_s(T)$ at 5 frequencies which exhibit very weak impurity scattering, indicative of the excellent quality of the $BaZrO_3$-grown crystals.

Chapter 3

Calibration and Checks for Systematic Errors

With the development of any new experimental technique comes a great amount of work in calibration and searching for systematic errors in the system. This chapter summarizes the results of the various experiments performed to this end. It should be pointed out here that the bulk of the effort with this apparatus until the present time has been along the lines of development of the technique.

3.1 Thermal Calibration

It is crucial that the thermal characteristics of the low temperature apparatus be well characterized for the successful operation of the bolometric measurement. In practice, this means that the temperature response of the sample and power meter stages with respect to incident power must be quantified. The calibration of each stage was achieved by supplying a known amount of sinusoidally oscillating power to the isothermal stage via the chip heater, and measuring the voltage across a resistance thermometer. The voltage signal is related to the thermal response and is measured with a lock-in amplifier referenced at the excitation frequency. The temperature response of the system then indicates the sensitivity in units of Kelvin per Watt. With this calibration, the absolute microwave power absorption of a sample can be inferred from the magnitude of the temperature oscillations which are induced in the isothermal stage. In addition to the explicit dependence on frequency contained in Eq. 2.2, the thermal response will also contain temperature dependence since $C \rightarrow C(T)$ and $\kappa \rightarrow \kappa(T)$.

The thermal response of both the sample stage and the power meter stage was measured at 1.2K as a function of frequency. The resulting data are shown in Fig. 3.1. With a long modulation period, the full thermal response of both the sample and power meter stages are obtained. In both cases, the limiting behaviour of the quartz glass tube and the stainless steel tube agrees with published data for thermal conductivity at 1.2K (sapphire:[25], stainless steel:[36]). As the period is reduced, the thermal penetration depth in the weak links decreases and the magnitude of the temperature oscillation is reduced. The data for the sample stage reveals two different time constants in the system. The first results in a corner frequency of roughly 2.86Hz (0.35s) which would correspond to the main structure of the quartz tube and sapphire block, and the second is at something above 10Hz (0.01s) which would be the thin sapphire plate. The data points on the power meter stage indicate only one time constant with a corner frequency near 4s. Note that the sensitivity of the stainless steel and copper assembly is approximately a factor of two lower than the quartz and sapphire stage at DC. As a further investigation, the thermal response of the sample stage was measured via heating with microwave power to ensure that no further time constants were introduced by the sample, grease, sapphire plate, and sapphire spacer combination. This independent calibration check also ensures that the heater is well anchored to the sapphire stage. It can be seen that there is no appreciable difference in the response whether the modulated power enters via the sample chip heater or via a sample suspended on a sapphire plate into the microwave field.

The choice of a modulation frequency of 0.45 Hz for the bolometric technique was made based on the data in Fig. 3.1. As described in chapter 2, the choice of modulation frequency was based upon obtaining the maximum possible sensitivity while minimizing the effects of 1/f noise. Although at 0.45 Hz the response of the power meter stage is already down by 9 dB, the signal due to the microwave power absorption by the metal is much greater than that generated by a YBCO sample and the loss in signal can be

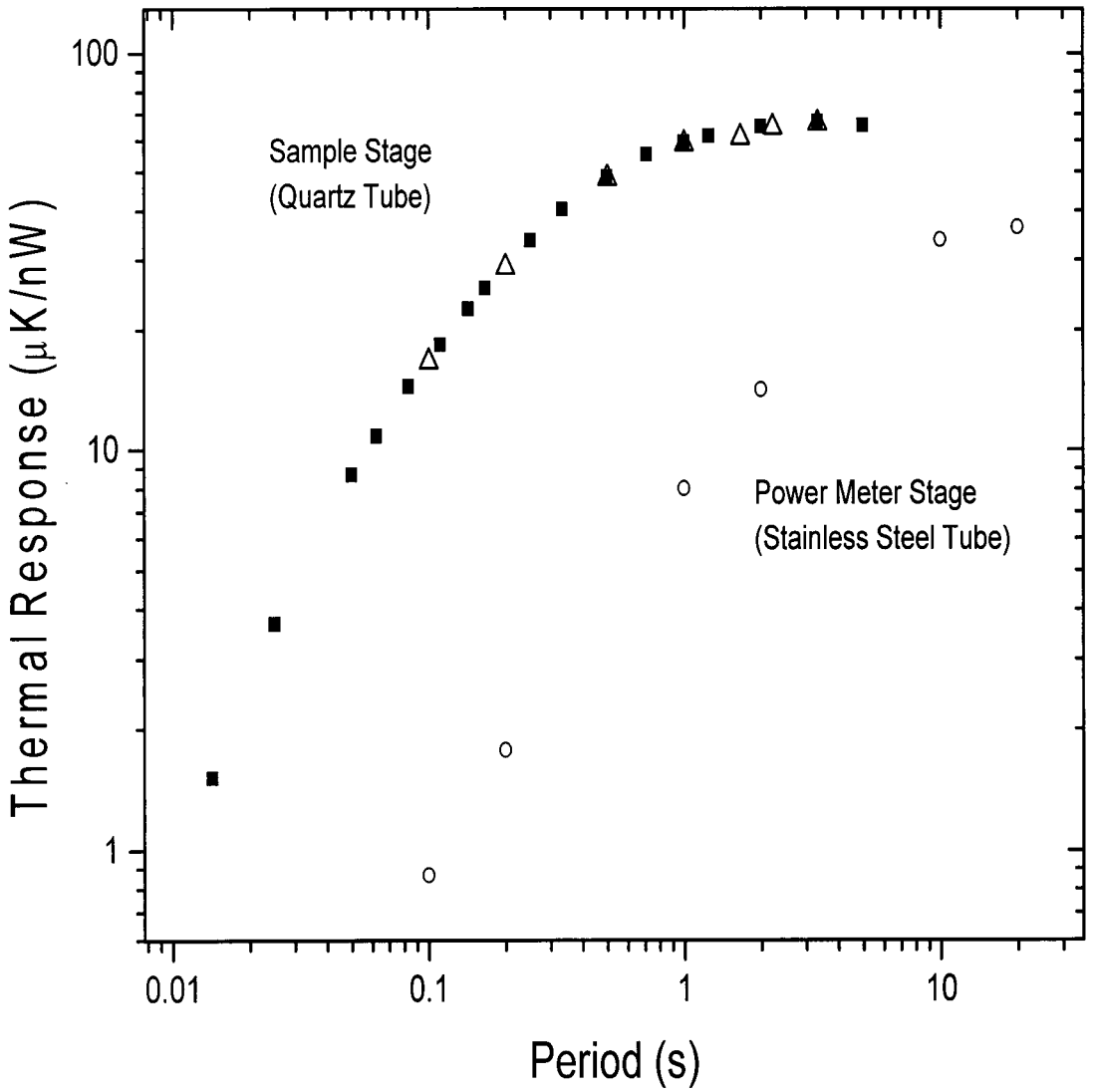

Figure 3.1: Frequency dependence of the thermal response of the sample and power meter stages at 1.2K. The low frequency limiting values are in good agreement with published data on the thermal conductivity of quartz glass and stainless steel. The open triangles are data taken using microwave radiation rather than the chip heater to induce the thermal oscillations. This ensures that no other relevant time constants exist in the system which would affect the calibration.

tolerated.

The process of thermal calibration is performed prior to each measurement. This is necessary to monitor subtle changes in thermal response between runs, and to ensure that the system is behaving normally. A variety of problems such as a change in the thermal response of weak links, bad thermometer contact, or a helium leak into the probe are easily detected in this fashion.

The temperature dependence of the thermal conductivity was also briefly examined for the quartz tube on the sample stage. This was done with only 4 data points, but yielded a result which is in moderate agreement with published data. It was found that κ varies as $11.0(T/K)^{2.2}\ \mu W/cmK$ in the range 1-2 K, while Stevens measured $14.7(T/K)^{1.87}\ \mu W/cmK$[25]. As he points out, this power law behaviour is typical for an amorphous solid at low T and is observed in many materials of this type.

3.2 Sample Alignment

The sapphire plate onto which the YBCO crystal is mounted is not permanently fixed to the sample holder, and hence the crystal must be carefully positioned before each run. An aluminum block which bolts to the sample pot provides a guide to the eye for alignment purposes. The mounting of the sample is done under a microscope, and cross hairs carved into the aluminum block indicate the optimal position.

Three measurements on the same crystal were made varying only the position of the crystal in order to investigate the effect of misalignment. There is very little room to move the sapphire plate laterally (the x or y directions in Fig. 2.2) since the tolerances with respect to the walls of the entrance hole are very tight. Therefore, only the distance the sample entered into the cavity (the z direction in Fig. 2.2) could be varied, *i.e.* along the end wall. The sequence of measurements began with the sample centred, then it was

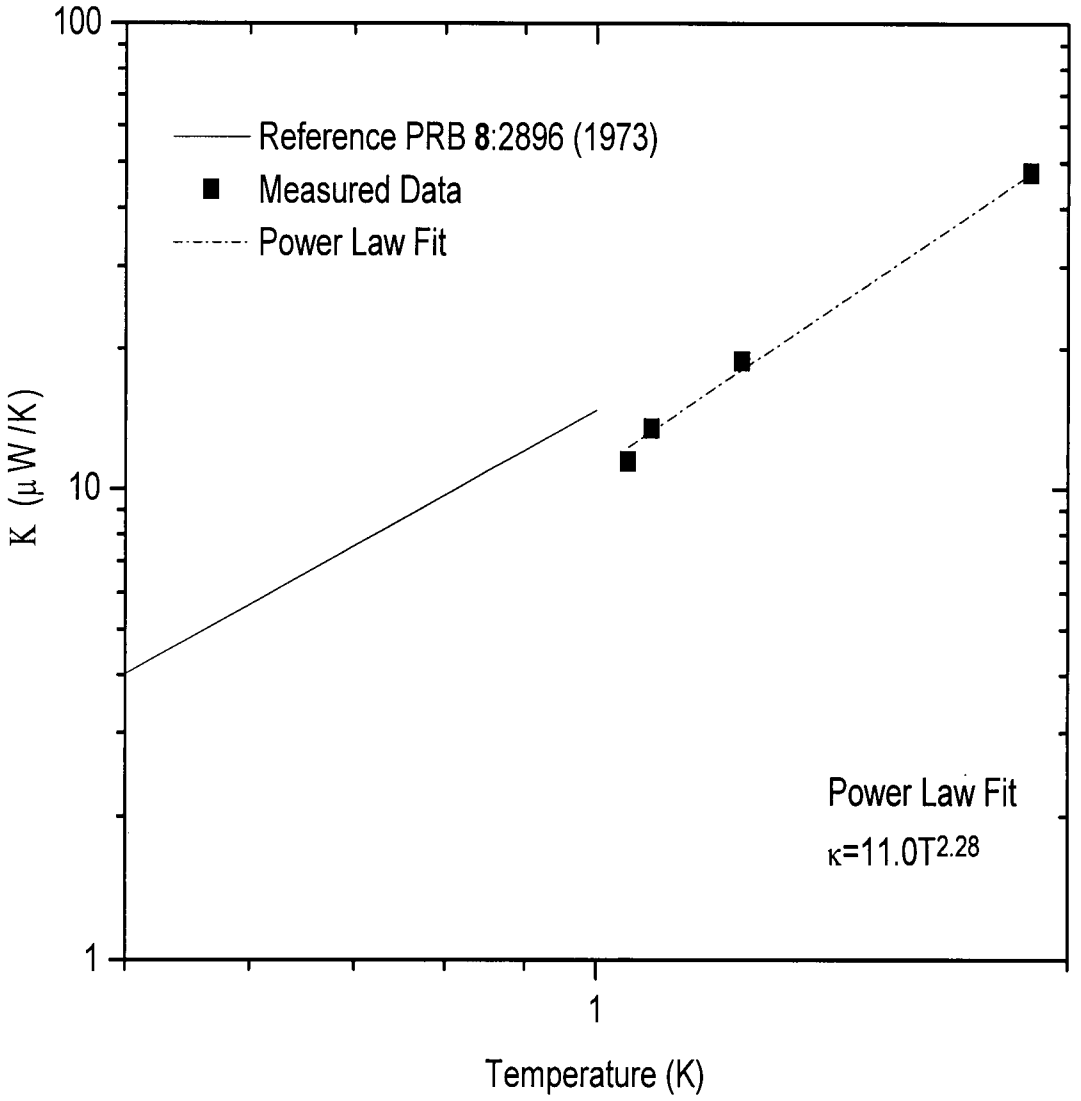

Figure 3.2: The temperature dependence of the thermal conductivity κ for the quartz tube on the sample stage ($A/\ell = 5.52\ mm^2$). The power law fit is reasonable, as is the agreement with the published data in Ref. [25].

moved to 0.25 mm before centre, and finally 0.5 mm past the centred position. This covers the range beyond what could possibly be encountered as alignment error. Since the typical sample dimension is less than 1mm on a side, a misalignment of 0.25 mm is very evident. The low frequency data showed very little change between runs, although the discrepancy proved to be noticeable above 10 GHz. The reason for the larger effect at high frequency is not clear. The magnitude of the variation was largest for the run with the sample farthest from centre affecting the measurement by roughly 10%. However, as stated previously, these tests were done on the worst case scenario, thus ensuring that errors due to variations in sample positioning during normal measurements would be sufficiently small.

3.3 Reference Material for Power Meter

The success of the power meter relies on the fact that a normal metal obeying the classical skin effect has a well known power dissipation in a microwave field as given by 1.17. Since the power meter is cooled to temperatures near 1 K, many metals are ruled out for use because they become superconducting. Also, high purity metals must be avoided since the electron mean free path becomes very long at low temperature and the metal enters the anomalous skin effect regime at microwave frequencies. Further explanation of this effect can be found in the books of Abrikosov[37] and Ziman[38]. This experiment requires a reference material which has a high chemical purity, is homogeneous, and is an alloy with enough scattering centres to be sure that R_s is substantial and that the electron mean free path does not put it into the anomalous skin effect regime.

The first choice of reference material used was stainless steel shim stock which is often used as a reference material at infrared frequencies. Eventually it was discovered that this was in fact a poor choice when working at microwave frequencies. Unusual anisotropic

behaviour was observed which seemed to point to magnetic susceptibility effects. Indeed the material was rather magnetically hard, and it is conceivable that the rolling of the shim stock was responsible for the anisotropy. In any case, the use of this material was quickly abandoned.

The search for a new reference material ended with the choice of an alloy of silver and gold. Both are readily available commercially at very high purity levels, and the two form a homogeneous alloy with a very simple phase diagram.[39] This alloy was prepared in-house at UBC, rolled to a suitable thickness, and cut to size.

Powders of silver and gold of 99.999% purity were mixed at a composition of 78 % atm silver (107.868 amu) and 22 % atm gold (196.967 amu). The mixture was heated above the melting point of $1000°C$ and the resulting material was quite malleable. The pellet which emerged from the furnace was pressed in a hydraulic press and then rolled to form a thin foil. The metal was shielded from contamination by acetate sheets when in the press and rollers, while frequent annealing at $900°C$ during pressing relieved work hardening. Small, roughly square samples were cut from the foil with a razor blade and then etched in 50% hydrochloric acid to remove any steel from the blade which may have contaminated the edges. The silver alloy was not noticeably affected by the etchant.

Since R_s is determined from the DC resistivity ρ of the metal, its measurement is crucial. This was accomplished by cutting a strip of foil and performing a careful four point measurement as a function of temperature. In order to determine ρ, the dimensions of the foil strip were required. The determination of the thickness of the strip proved to be one of the limiting factors in the absolute accuracy of the calibration of this experiment. Via two different measurements, one using a sensitive digital micrometer and another using a density measurement approach, the thickness was found to be $34\mu m \pm 10\%$. This uncertainty of 10% is the dominant experimental uncertainty in the determination of R_s for any superconducting sample. The resistivity data is shown in Fig. 3.3. The

value of ρ shows very little temperature dependence below 30K all the way down to 1.8K, settling into a value of $6.38\mu\Omega - cm \pm 10\%$.

The value of R_s calculated via 1.10 assumes the thick limit for field penetration, where the thickness t of the metal slab is much greater than the skin depth ($t \gg \delta$). When the skin depth approaches a value equivalent to half the thickness of the slab, the fields penetrate enough of the sample that there is no longer the simple case of screening currents flowing on the surface, and the power absorption is reduced. At lower frequencies where the skin depth increases[1], the absorption by the metal is reduced by thin limit effects. The factor by which the absorption is decreased is derived in appendix C to be

$$\frac{P_{thin}}{P_{thick}} = \left[\frac{\sinh\left(\frac{t}{\delta}\right) - \frac{t}{\delta}}{\cosh\left(\frac{t}{\delta}\right) - 1}\right] \tag{3.1}$$

and the measured power absorption at each frequency must be divided by this factor. For this experiment, only the very low frequency data (<0.5 GHz) proved to be susceptible to this effect, and it is at most a 1% correction.

3.4 Grease and Sapphire Background

Background signal arising from dielectric losses due to the sapphire plate which suspends the sample in the magnetic field, and the small amount of silicone vacuum grease used to hold the sample were measured. The thermal technique used for this experiment means that any form of dissipation will give rise to additional signal. Although the apparatus was designed with the intention that the samples would be positioned near the end wall where the electric fields should be minimized, the possible effects of the electric fields deserves attention. As previously mentioned, sapphire is known to have low dielectric loss, and from experience with other cavity perturbation techniques it is also known that

[1] 4μm @ 1 GHz, 1.3μm @ 10 GHz for the Ag:Au alloy

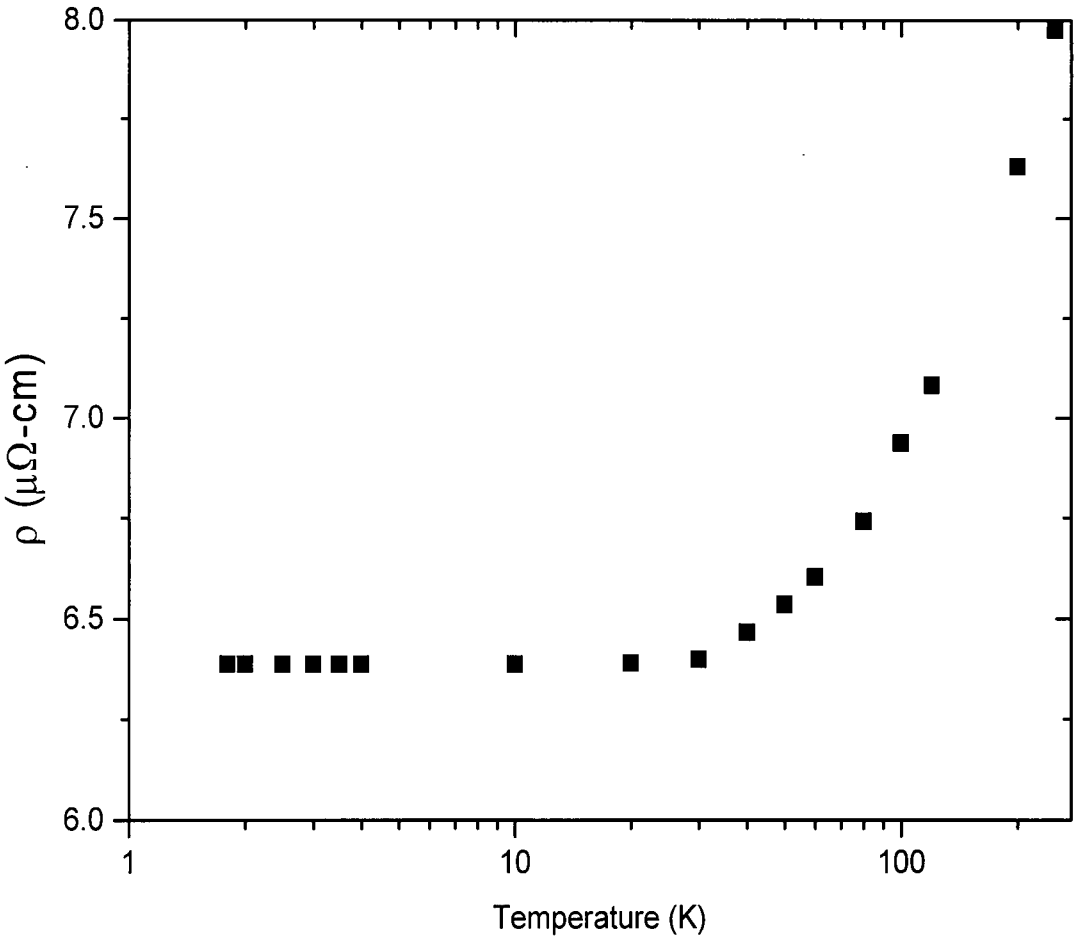

Figure 3.3: Temperature dependence of the resistivity of the silver/gold alloy. The resistivity is temperature independent below 30K with a value of $6.38\mu\Omega - cm \pm 10\%$. The uncertainty arises from the inability to precisely determine the thickness of the foil sample.

the loss of silicon grease is quite low[14].

A measurement of the bare sapphire plate over the full frequency range did not provide any measurable signal. An amount of vacuum grease, typically of that used to mount the sample was then added and the measurement repeated. In this case, a small signal was observed which increased with frequency, as expected for dielectric loss. This signal is not negligible and reaches a value of nearly 10% of the loss of a YBCO crystal at the high frequency end. However, this background calibration is probably not accurate since the field profile at the tip of the sapphire where the grease lies is distorted by the superconducting sample itself. A further experimental test was carried out, where a YBCO crystal was measured, additional grease was added to the top surface of the crystal, and the measurement repeated. In this case no noticeable change in signal was observed, which indicated that the loss due to the grease is reduced by the presence of the superconducting sample. The conclusion from these measurements is that the background signal is sufficiently small to justify its neglect. The data discussed above is given in Fig. 3.4.

3.5 Microwave Field Amplitude Calibration

Once the apparatus had been constructed and the thermal characteristics understood, the next step was a calibration with identical materials on the sample and power meter channels. A frequency independent ratio ensures that systematic errors are not a problem, while the magnitude of the absorption on the two sides calibrates the magnetic field strength incident upon the sample and reference material positions. Many attempts and much troubleshooting were devoted to this task. It is through these investigations that the problems with the stainless steel reference material were uncovered and that it was realized that the DC temperature of the reference stage was fluctuating during early runs

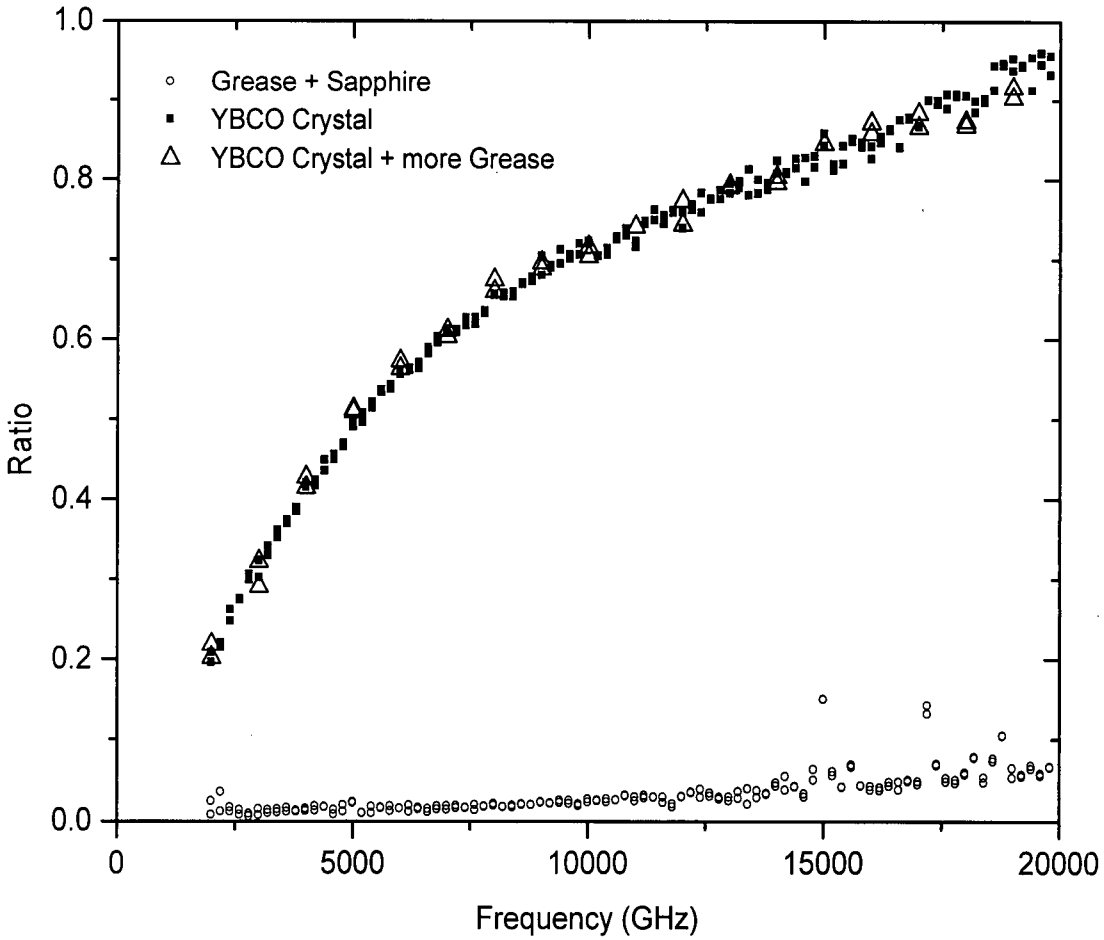

Figure 3.4: Two measurements examining the effect of a grease and sapphire background signals. The data is presented as the ratio of sample to power meter signal. The first is a measurement of the sapphire plate with an amount of grease typically used to mount a YBCO sample. The second is a comparison between a measurement of a YBCO sample and a repeated measurement with an additional amount of grease added to the top surface of the sample.

with the apparatus.

Fig. 3.5 presents the raw voltage signals collected during a field calibration run. The signals directly correspond to the magnitude of the temperature oscillations on the two thermometers. The "constant signal level" option in the software (see section 2.6) has been set to maintain the sample signal at 10 mV, resulting in a wide spectroscopic region over which the sample signal has a constant amplitude.

Fig. 3.6 shows two measurements of this sort, with samples of the silver/gold alloy reference material on both channels. The ratio shown in the plot is corrected for the difference in areas between the pieces of alloy placed on the sample and power meter stages. In order to rule out geometric effects, two runs were done with different sized pieces on the sample side, without altering the piece on the power meter. Both data sets are quite flat over nearly all of the broadband 20 GHz sweep. The data is particularly flat for the larger sample ($0.691 mm^2$, flat to within 1%) while there is a gentle positive linear slope in the data for the smaller area sample ($0.288 mm^2$, flat to within 4%). Both data sets also exhibit upturns at low frequency, and dips near 12 GHz and 19 GHz. An explanation for the increasing slope, the upturn and dips remains to be found, though they seem to be correlated with where the signal on the sample channel becomes exceedingly small. Nonetheless, these are very minor anomalies in the data, but they will be kept in mind when examining measured data from superconducting samples. Based on the data on the larger sample in Fig. 3.6, which is closer to the size of the YBCO samples typically measured, subsequent measurements are corrected for the difference in field amplitude by dividing out a constant value of $0.78 \pm 1\%$.

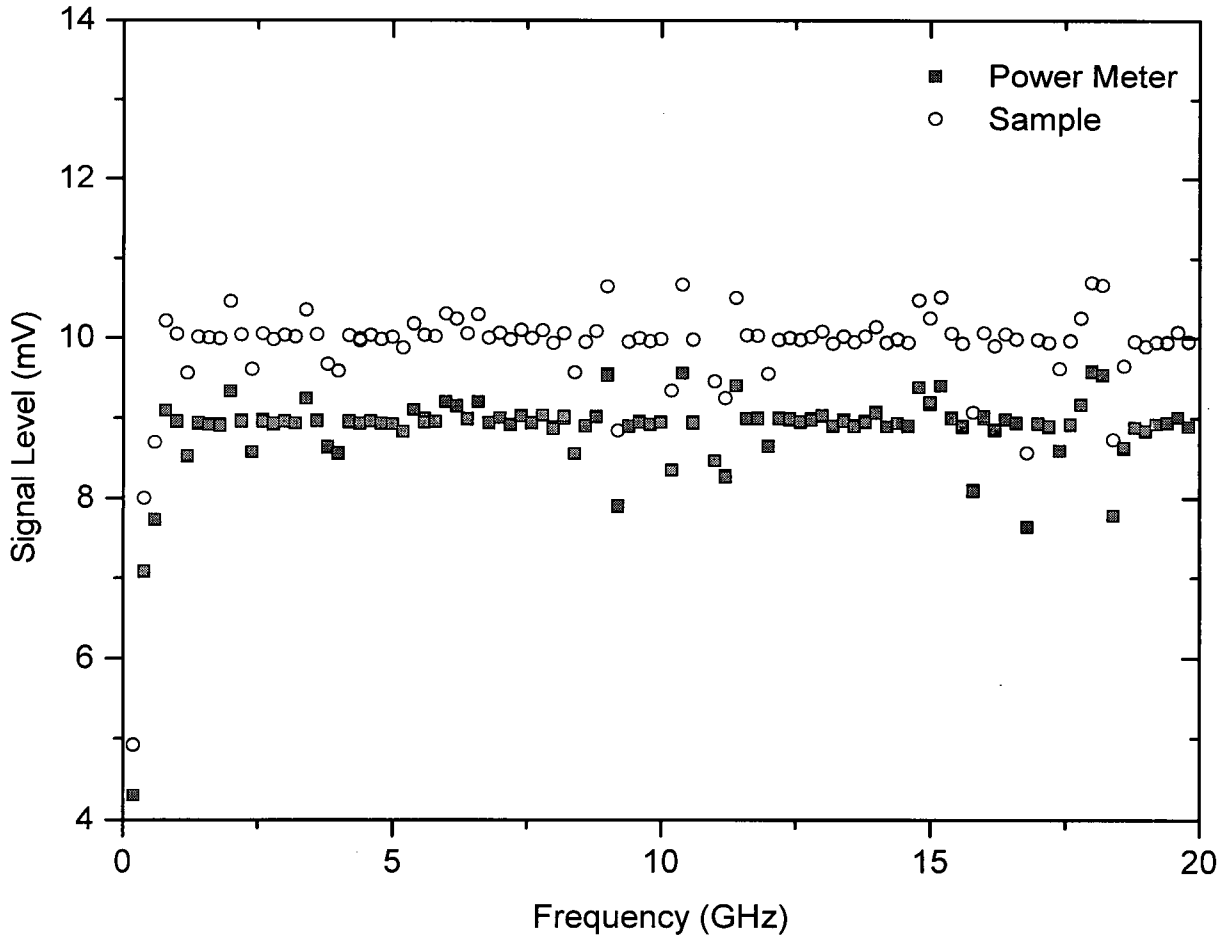

Figure 3.5: Raw voltage signals for sample and power meter bolometers during the measurement of two pieces of silver/gold alloy. These signals correspond to the magnitude of the microwave absorption induced temperature oscillations. The scatter in the data is not noise, but is a result of the variation in microwave power due to standing waves and reflections down the transmission lines. The data collection software attempted to maintain a constant sample signal level of 10 mV during the sweep.

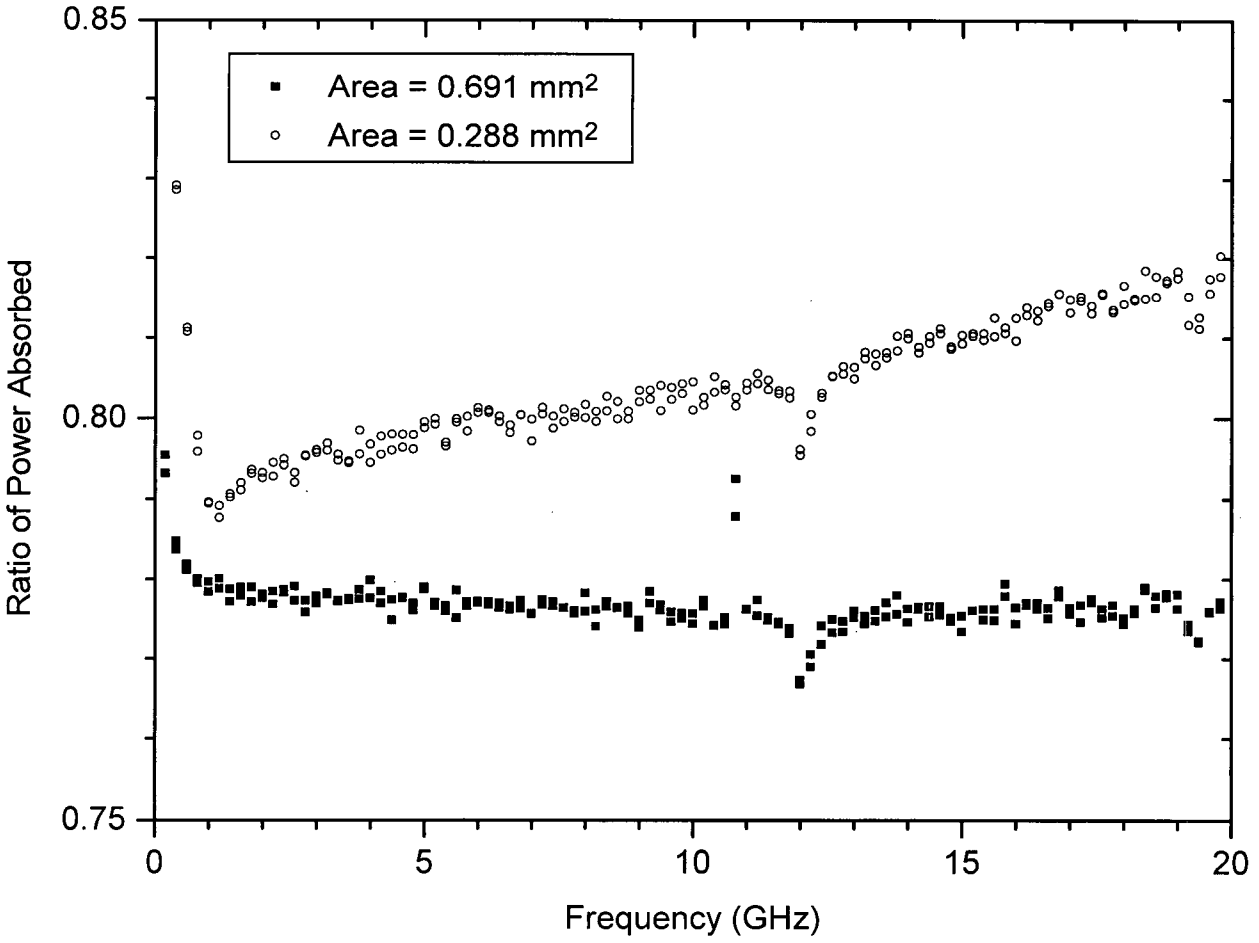

Figure 3.6: Measurement of silver/gold alloy on both sample and power meter stages. Identical materials on the two channels should yield a frequency independent signal, as is seen to be the case down to the few percent level. The origins of the slightly positive slope for the smaller sample and the dips in the data at 12 GHz are unknown. The ratio is less than unity since the septum is offset from the centre of the cavity, thus resulting in slightly stronger magnetic field intensities at the power meter sample.

Chapter 4

Data Analysis and Discussion

This chapter presents the measurement of the ab-plane surface resistance from 0.01-22 GHz of two detwinned oxygen overdoped YBCO samples (O=6.993). The two nominally identical samples exhibit features which agree qualitatively. However, there are also discrepancies which have received further investigation. However, they have not been satisfactorily sorted out at the time of writing. One of the samples was previously measured at 5 different frequencies by cavity perturbation in the UBC superconductivity lab, and this data is compared to the bolometric broadband measurement. R_s measurements were converted to conductivity assuming local electrodynamics and independently measured values of λ_o. A Drude spectrum was fitted to the $\sigma_{1(a)}(\omega)$ data for further comparison with the physical picture inferred from the cavity perturbation data.

4.1 ab-plane Measurements of R_s on $YBa_2Cu_3O_{6.993}$

Fig. 4.1 presents the raw signals recorded over the course of a frequency sweep. The YBCO signal level was nominally regulated at 50 mV, and since $R_s^{metal}(\omega) \propto \sqrt{\omega}$ and $R_s^{YBCO}(\omega)$ increases faster than $\sqrt{\omega}$ the signal on the power meter channel decreased as a function of frequency. The frequency variation of the absorbed power by the power meter will not alter the sensitivity of the stage because its DC temperature is regulated at a constant value. Both at the low and high frequency ends of the spectrum, the signal level is seen to drop below the 50 mV setpoint. At the low frequency end this is due to the very low absorption of the metal and YBCO sample. The high frequency roll off arises

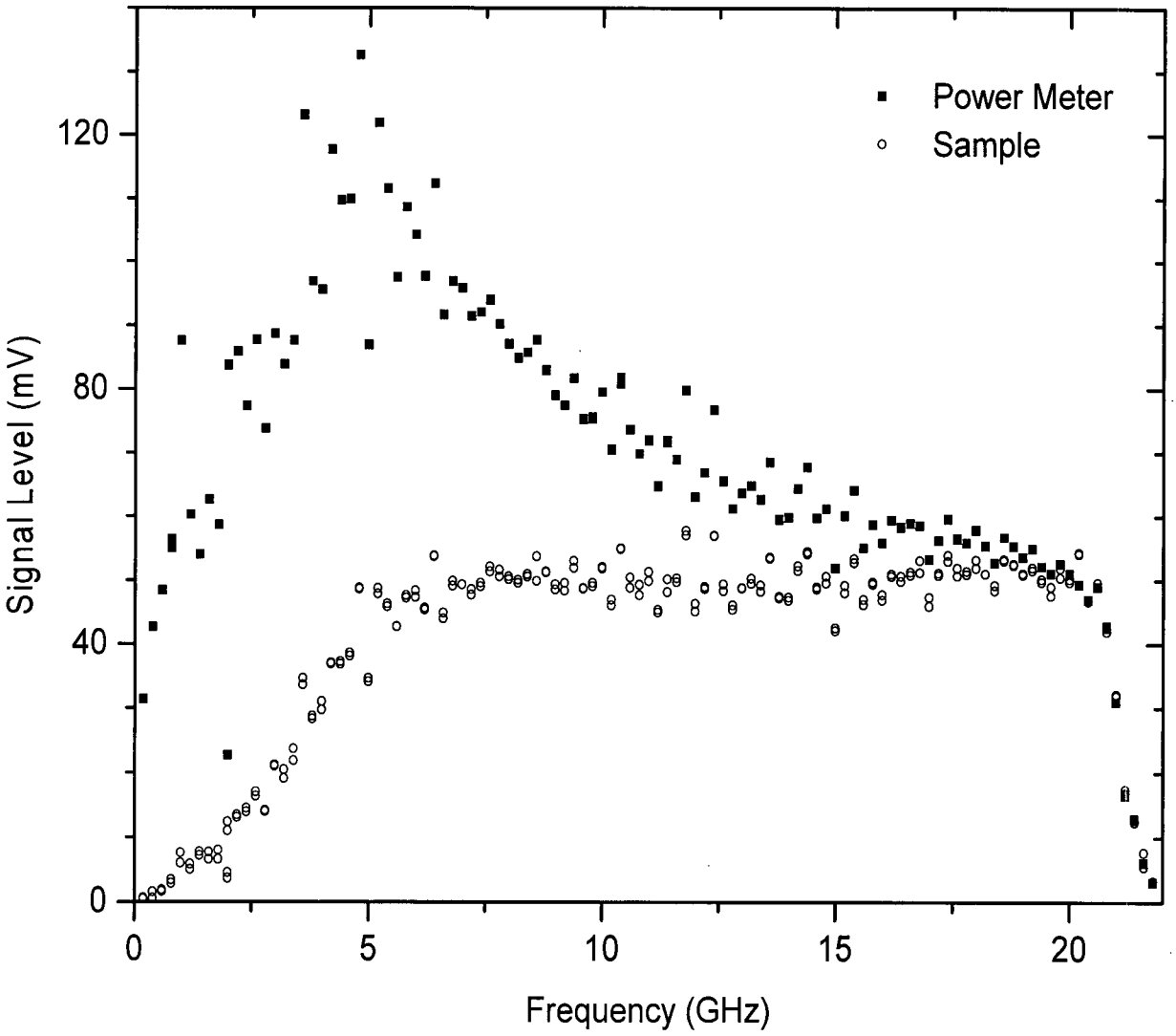

Figure 4.1: Raw voltage signals for sample and power meter bolometers during the measurement of sample YPH. The data collection software attempted to maintain a constant sample signal level of 50 mV during the sweep, however this was not possible at low frequency where the YBCO loss is very small. At high frequency the signal drops off above the maximum frequency of the microwave amplifier.

from the drop in the gain of the HP 8349B amplifier when the frequency exceeds the maximum specified operating frequency of 20 GHz. R_s is calculated from these voltage signals according to the following procedure:

1. Multiply raw voltage signals by thermal sensitivity calibration factors to convert voltages to absorbed power.
2. Correct power meter signal for thin limit effects as per equation 3.1.
3. Calculate the ratio of the absorbed power between the two sides.
4. Correct for field amplitude difference between two sides using the constant from the metal vs. metal data on larger sample from Fig. 3.6.
5. Calculate value of R_s^{metal} using equation 2.1.
6. Calculate R_s^{YBCO} from ratio of the absorbed powers and equation 2.1.

Fig. 4.2 shows $R_{s(a)}$ and $R_{s(b)}$ of sample YPH measured at T=1.3K. This crystal is 24μm thick in the $\hat{c}$-axis direction. Although some of the edges did not cleave cleanly, the shape is roughly rectangular in the ab-plane with $\ell_a \simeq 0.89$mm and $\ell_b \simeq 0.72$mm as measured via an optical microscope. A careful estimate of the total surface area yields a value of $0.646mm^2$. The $\hat{a}$-axis data was taken first, the experiment warmed to room temperature, the crystal was rotated without removal from the sapphire plate and cooled again for a repeat experiment to measure the $\hat{b}$-axis losses.

The data presented here has two data points per frequency, except at 2 GHz where there is an overlap between two data sets separately taken using the low and high frequency microwave amplifiers. The spread in the two data points gives a feeling for the signal to noise ratio (S:N) at each frequency, and hence the points have not been averaged. The data is of very reasonable quality over the majority of the spectrum. However,

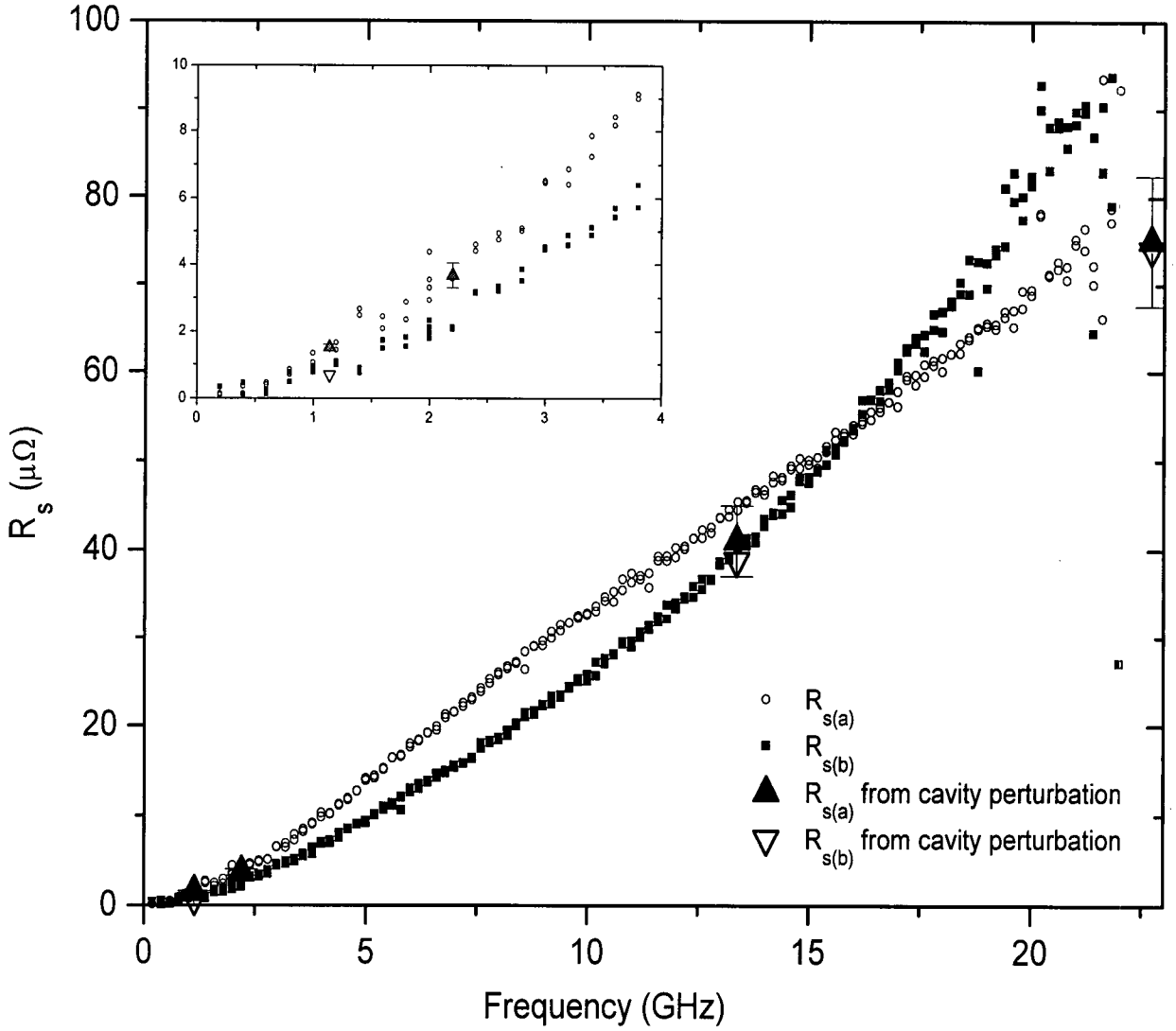

Figure 4.2: Initial measurement of an oxygen overdoped 24μ m thick YBCO sample YPH at T=1.3 K. $R_{s(a)}$ and $R_{s(b)}$ are easily seen to have different frequency signatures within the resolution of the instrument. Good agreement with cavity perturbation measurements of the same crystal at 1.1, 2.2, 13.3, and 22.7 GHz is apparent.

both at the low and high frequency ends the S:N is quite low. It is believed that this is simply due to the low microwave power level in the cavity at these frequencies. No attempt should be made to interpret any detailed physics in the data below 4 GHz, but it is included for completeness' sake.

$R_{s(a)}$ is seen to be predominantly linear over most of the 20 GHz wide spectrum with the onset of a slight power law curvature below about 10 GHz. $R_{s(b)}$ is rather different, exhibiting power law behaviour over the entire range with an exponent ~ 1.5. It is interesting to note that $R_{s(a)} > R_{s(b)}$ below a crossover frequency (f_{ab}) of 16 GHz. The crystal YPH is the same crystal measured using 5 different microwave resonators by Hosseini *et al.*[8] operating at 1.1, 2.2, 13.3, 22.7 and 75.4 GHz. This data was presented in Fig. 2.10. Their 1.2 K data, the lowest temperature attainable with the pumped helium-4 bath used by these experiments, is compared to the broadband measurement. At this temperature, very little can be said about the anisotropy from the cavity perturbation data due to uncertainty in the calibration of these experiments. The uncertainty in their data due to non-perturbative effects and systematic errors in calibration factors is indicated by error-bars on the data. However, the consistency in R_s over the spectrum between the two completely different measurement techniques is quite impressive. Note that there is no $\hat{b}$-axis data available at 2.2 GHz.

Not included on this plot are the 75 GHz data. The measured values of $R_{s(a)} = 700 \pm 10\ \mu\Omega$ and $R_{s(b)} = 1100\ \mu\Omega$ indicate a similar low temperature ab-anisotropy to the frequency swept data, *i.e.* $R_{s(b)} > R_{s(a)}$. While these values would be difficult to reconcile with an extrapolation of the bolometry data in Fig. 4.2, it is not inconceivable that other effects come in to play at high microwave frequencies. In particular, the increasing importance of a normal fluid contribution to the screening currents at high frequencies may alter the curvature of $R_{s(a)}$ and $R_{s(b)}$ considerably, thus making any extrapolations of the bolometry data highly suspect.

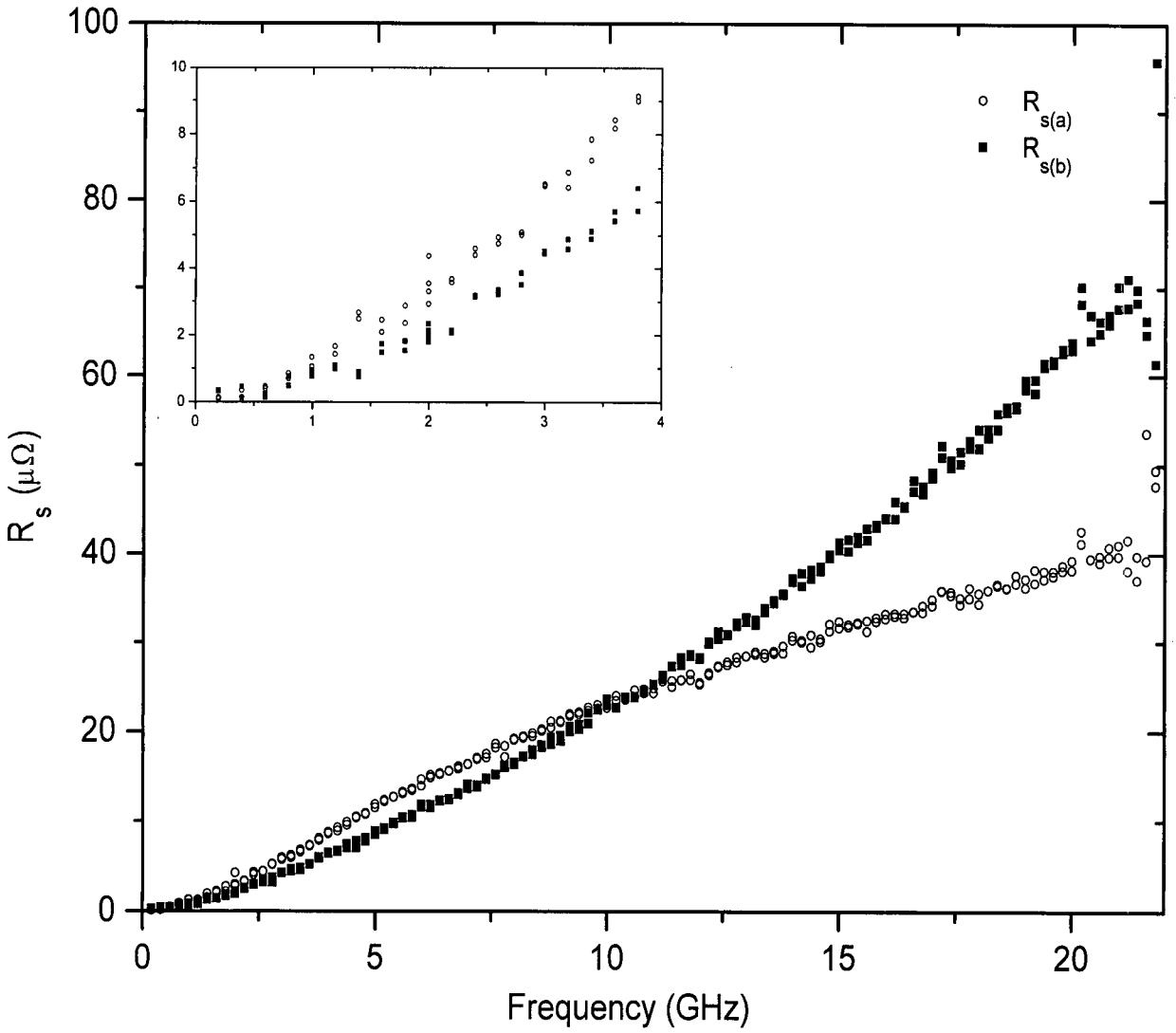

Figure 4.3: Initial measurement of an oxygen overdoped 6.5 μm thick YBCO sample named YOV. This is the lowest loss crystal measured to date with this experiment.

Fig. 4.3 presents data for the sample YOV at T=1.3K. The $0.905mm^2$ ab-plane area of this crystal is 40% greater than that of YPH. The edges of this crystal are very straight with $\ell_a = 0.89$ mm and $\ell_b = 1.02$ mm. The $\hat{c}$-axis dimension is 6.5 μm.

Qualitatively, this data looks similar to that of YPH. Again, at low frequency $R_{s(a)} > R_{s(b)}$ up to the frequency f_{ab} above which $R_{s(b)} > R_{s(a)}$. The $\hat{b}$-axis data shows power law curvature with an exponent of $\sim$1.4 up to 12 GHz, beyond which a fairly linear region sets in. $R_{s(a)}$ is quite linear above 10 GHz, but exhibits some curvature below this frequency which is not well described by a power law. The most striking difference between this data and that of Fig. 4.2 is the reduction in magnitude of both $R_{s(a)}$ and $R_{s(b)}$. The frequency dependence has also changed, particularly in the $\hat{a}$-axis data where YOV does not have the broadband linear region of YPH. The YPH data had f_{ab}=16 GHz whereas in the YOV data, f_{ab} has now shifted down to 11 GHz. These differences are quite significant.

4.2 Repeatability Study - Degraded Surface Issues?

At this point, measurements from two oxygen overdoped single crystal YBCO samples have been presented. The overall features of the two measurements agree qualitatively, however they display some disturbing discrepancies. The most mysterious aspect is the variation of R_s at high frequency of up to 50% between samples. This result was not consistent with our observing intrinsic behaviour, and further experimental attention was required.

To this end, a study of the repeatability of the measurements on the crystal YOV was undertaken. It must be noted that the cavity perturbation techniques which measure $R_s(T)$ are unable to resolve the low temperature residual loss to very high accuracy. Since microwave measurements probe below the sample surface to a depth set by the

penetration depth, they are therefore very sensitive to the surface quality. One would expect the residual loss to be easily enhanced by degraded surfaces.

Measurements of $R_s(T)$ at 22 GHz on YPH and YOV over the temperature range $5K < T < 80K$ were indistinguishable before this study began. The following story has unfolded with the broadband measurements of R_s on YOV, and the corresponding data is shown in Fig. 4.4.

One factor which requires attention is the presence of a thin layer of Non-Aq stopcock grease on the two samples. This grease is used by two of the cavity perturbation measurements in the UBC superconductivity lab because it has been observed to have lower dielectric losses than silicone grease at higher temperatures. Following a period of several days after application to a YBCO crystal, the Non-Aq becomes hard and very difficult to remove from the sample. This is not the case with silicone vacuum grease which is easily removed with heptane and gentle friction. Both YPH and YOV samples had thin coatings of non-aq covering most of one crystal face during the initial bolometry measurements. Based on the cavity perturbation measurements there was no reason initially to suspect that this grease contributed to an increased dielectric loss, but over time the question was raised.

$R_{s(a)}$ and $R_{s(b)}$ data from run #1 with YOV were already shown in Fig. 4.3. Both sets of data represent the lowest measured loss with this experiment to date. As a repeatability check, the sample was then removed from the experiment and cleaned to remove the silicone vacuum grease in the standard manner with a small amount of heptane and a low lint tissue. The sample was then remounted and measurement #2 performed. Good agreement between these two runs is seen at the low frequency end of the spectrum, however above 8 GHz the new loss is higher. The discrepancy increases with frequency, reaching a value as much as 30% above the first run.

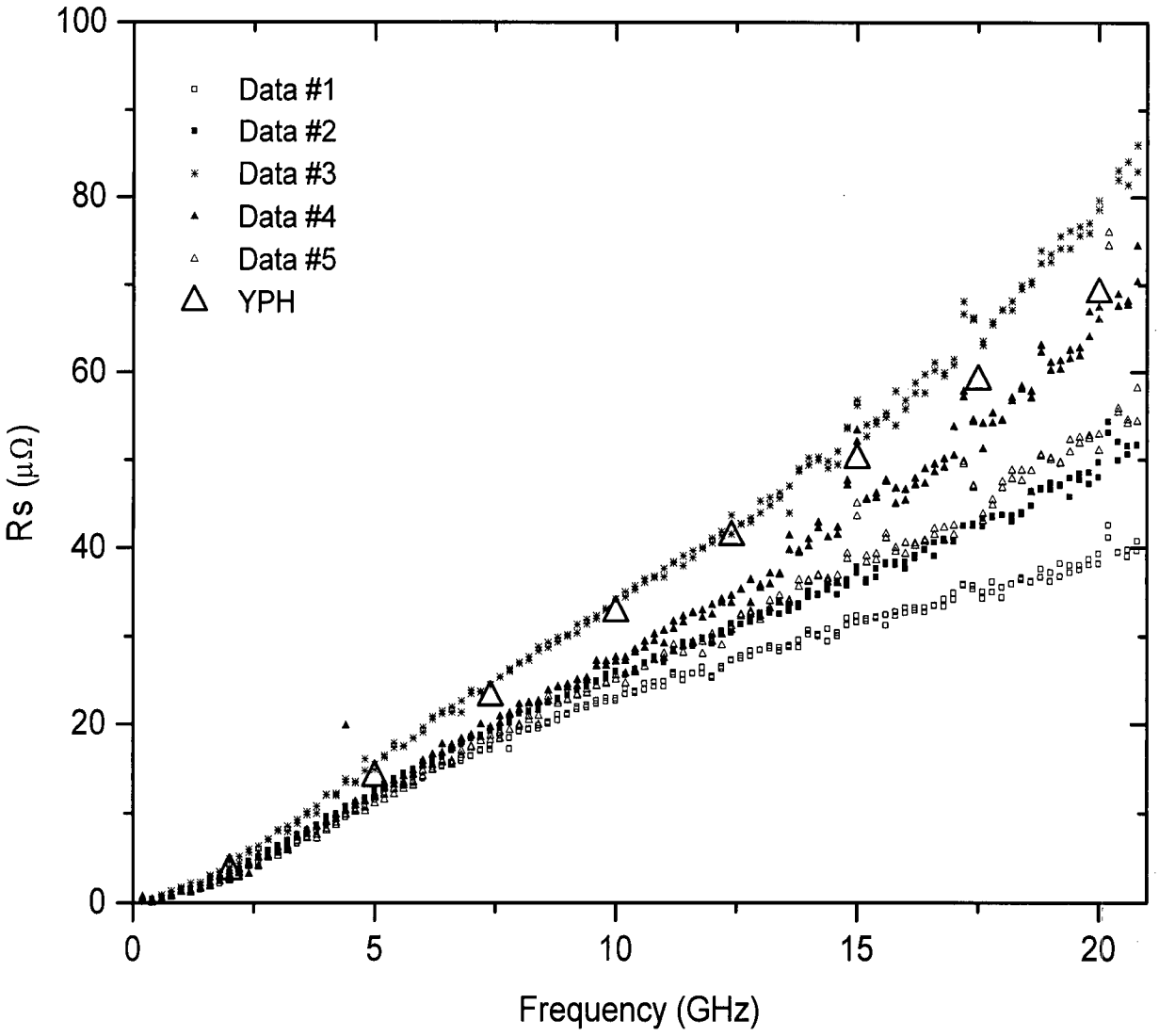

Figure 4.4: Variations in $R_{s(a)}$ of YOV sample between runs at 1.3K. The numbered data sets are in chronological order. Note that the crystal was broken between data #2 and #3. The measurement with the highest loss #3 shows good quantitative agreement with the sample YPH. Subsequent chemical etching of the surface before runs #4 and #5 served to reduce the loss near to the level seen initially. Refer to the text for the complete details.

The immediate suspicion was that the increased high frequency loss was due to absorption of a dielectric contaminant on the surface. The sample was removed and cleaned very thoroughly with acetone followed by heptane, again using standard procedure. Unfortunately, during cleaning the crystal was accidentally cleaved into a number of pieces. The largest remaining fragment had approximately 1/3 the ab-plane surface area of the initial sample. The new dimensions were measured to be $\ell_a = 0.89$mm and $\ell_b \simeq 0.36$mm with a total area of $0.32mm^2$. It is worth noting that because ℓ_a remained unchanged, the $R_{s(a)}$ to $R_{s(c)}$ admixture ratio has been preserved.

Measurement #3 showed markedly different frequency dependence of $R_{s(a)}$ with a factor of two increase in magnitude at 20 GHz from measurement #1. The spectroscopic feature of a linear $R_{s(a)}$ up to 13 GHz appears again, remarkably similar to that observed with the other crystal, YPH. Selected YPH data points from Fig. 4.2 are included for comparison in Fig. 4.3. Recall that the metal versus metal calibrations were not highly sensitive to the area of the sample used and hence one gains confidence that the effect seen here cannot be simply due to the reduction in crystal area.

To permit a careful comparison between YOV and YPH, the YOV crystal was rotated to repeat the $\hat{b}$-axis measurement. If an extrinsic effect had altered the measurement, it should be apparent in both $\hat{a}$ and $\hat{b}$-axis data. Fig. 4.5 reveals that the complete ab-plane R_s was very similar between the two crystals up to 17 GHz and f_{ab} has recovered the value of 15 GHz, close to the 16 GHz of YPH. There is some high frequency disagreement between the two crystals, but on a much more tolerable level. One difference between the two crystals which might possibly considered to resolve this discrepancy is the $\hat{c}$-axis thickness, $t_{\rm YPH} = 24\ \mu$m and $t_{\rm YOV} = 6.5\ \mu$m. The total apparent $\hat{a}$-axis surface resistance value measured with this experiment will always be

$$R_{s,\text{apparent}} = R_{s(a)} + \frac{t}{\ell_a} R_{s(c)}. \tag{4.1}$$

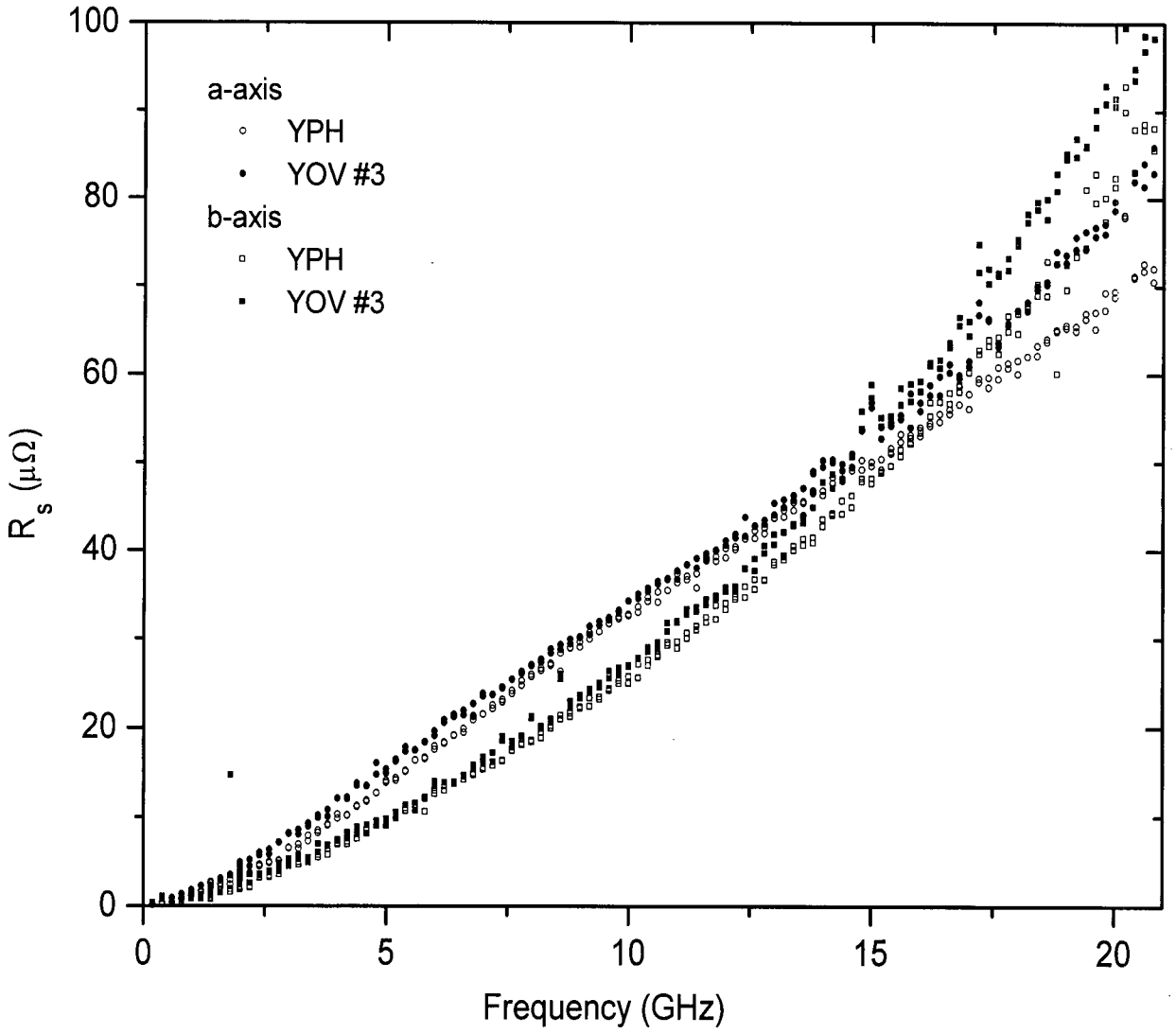

Figure 4.5: A comparison of YPH and YOV data #3, the measurement with the highest loss. Very good agreement is seen for both $\hat{a}$ and $\hat{b}$-axis data up to 17 GHz, above which YOV is greater than YPH in both cases.

Based on the $R_{s(C)}$ numbers from Hosseini and Harris that were given in section 2.1 and the geometry of these crystals, the $\hat{c}$-axis contribution is expected to be on the order of 5 $\mu\Omega$ for YPH and 1 $\mu\Omega$ for YOV. In contradiction to this, Fig. 4.5 has $R_{s\mathrm{YOV}} > R_{s\mathrm{YPH}}$.

Three consecutive data sets in which the loss increased significantly between each run led to the suspicion that some cumulative surface degradation was occuring. Furthermore, the agreement between YOV and the already well-handled sample YPH at this point seemed to present a fairly strong case for this scenario. A method was required to remove the extrinsic losses and recover the intrinsic value. Two possible explanations were postulated for the variation in the loss. The first is the surprising possibility that the YBCO crystal surface degraded over time, possibly by chemical treatment. The second is that the Non-Aq grease has been altered chemically between runs, and somehow became more lossy with each successive handling.

A recent experiment has been performed by a member of the UBC superconductivity group on wet chemical etching the surface of a YBCO crystal following mechanical polishing[40]. Using $R_s(T)$ measurements and an atomic force microscope as characterization tools, the results indicated that the surface quality can be recovered by removing an outer layer from severely damaged crystals. The etch rate for 0.5 % Br in ethanol solution was examined empirically and was found to be highly sample dependent. The rate at which material is removed in the ab-plane was unobservably small, and can be quantified at <100 Å/min. The $\hat{c}$-axis rate was <1000 Å/min. The solution preferentially etches dislocations in samples such as damage introduced by mechanical polishing, and thus the etch rate in any given sample will depend highly on the crystalline quality of the sample.

Following measurement #3, the sample was etched in the Br solution described above. The goal was to remove both of the possible symptoms described above which would act to increase the loss. The etching was continued until a significant portion of the Non-Aq

grease was removed. Following a total etch time of 50 minutes, little Non-Aq was visible and there were some easily identified square edge pits in the crystal surface. These pits covered a small fraction of the total surface area (<1 %).

Measurement #4 was made following the 50 minute etch. R_s had decreased through the entire frequency spectrum as compared to trial #3, partially recovering the initial measured value. Given this desirable result, the sample was etched for a further 15 minutes bringing the total etch time to 65 minutes. The second etch removed nearly all traces of the non-aq grease visible under the optical microscope. The final measurement, #5, again exhibits a further reduction in the loss. The level returned to within 30 % of the first measurement, with the discrepancy still the greatest at the upper end of the frequency range. The end result is a measurement which looks much more similar to data #1 than to data #3.

It seems that the bolometric technique is under control since the series of five measurements hold together in a consistent fashion. Despite this, it is difficult to draw concise conclusions from this study. It has become apparent that the residual loss is somehow varying on the level of these measurements. Further experiments with samples which have not been previously handled would be illuminating, as would performing a similar etching procedure on the YPH sample. Clearly, more work is required to determine a confident estimate for the level of the residual loss. The sequence of measurements described above leads one to believe that the data most representative of *intrinsic* behaviour is that with the lowest loss, *i.e.* the data set #1 on YOV.

4.3 Conductivity

The measured surface resistance data can be converted to conductivity according to equation 1.13. The value for λ_o has been taken from FTIR spectroscopy measurements

by Basov *et al.* to be $\lambda_{o(a)}$=1600 Åand $\lambda_{o(b)}$=1030 Å[18]. Their data cannot resolve a frequency dependence of λ_o below 500 cm^{-1} (15 THz).

Fig. 4.6 presents both $\hat{a}$ and $\hat{b}$-axis conductivity values for YOV measurement #1. Immediately, the poor S:N ratio below 3 GHz draws attention. A Drude model fit to the $\hat{a}$-axis data above 3 GHz seems to capture the main features of the spectrum. As the frequency is reduced below 3 GHz, it is unclear from the data whether the conductivity levels in a manner consistent with the Lorentzian lineshape, or continues to climb more steeply. The Drude fit given in Fig. 4.6 provides a normal fluid oscillator strength of $ne^2/m_n^* = 2.5\times10^{17}$ $(\Omega^{-1}m^{-1}s^{-1})$ and a quasiparticle scattering time of $\tau = 2.4\times10^{-11}$ s. These are consistent with the results of Hosseini *et al.*[8] who extracted a temperature independent (for T<20 K) scattering time of $\tau = 1.8(\pm0.2) \times 10^{-11}$ s and an ne^2/m_n^* value which extrapolates to $\sim 3 \times 10^{17}$ $(\Omega^{-1}m^{-1}s^{-1})$ at 1.3 K. Further detailed analysis of the bolometry data will be reserved until the surface issues have been resolved.

$\sigma_{1(b)}(\omega)$ is roughly an order of magnitude larger than $\sigma_{1(a)}(\omega)$ across the spectrum, which is interpreted as an enhancement of the conductivity in this direction by the *CuO* chains. The high frequency $\sigma_{1(b)}(\omega)$ seems to plateau at a value of approximately 10^7 $\Omega^{-1}m^{-1}$. This plateau indicates an increased oscillator strength beyond 10 GHz which cannot be accommodated by a Drude model. The mechanism which is responsible for this enhancement is unclear at the present time, and is the topic of further research at UBC.

The prediction for the universal low temperature conductivity limit, which will set in below a temperature T^*, is $\sigma_{oo} = ne^2/\pi m\Delta_o \sim 3 \times 10^5$ $\Omega^{-1}m^{-1}$[12]. Note that this calculation does not include Fermi liquid and vertex corrections which have recently been proposed to contribute a significant enhancement to σ_{oo}[41]. Harris[11] has shown that the low temperature extrapolation of the microwave conductivity data of Hosseini *et al.*[8] produces a residual conductivity which is frequency dependent and has a high frequency

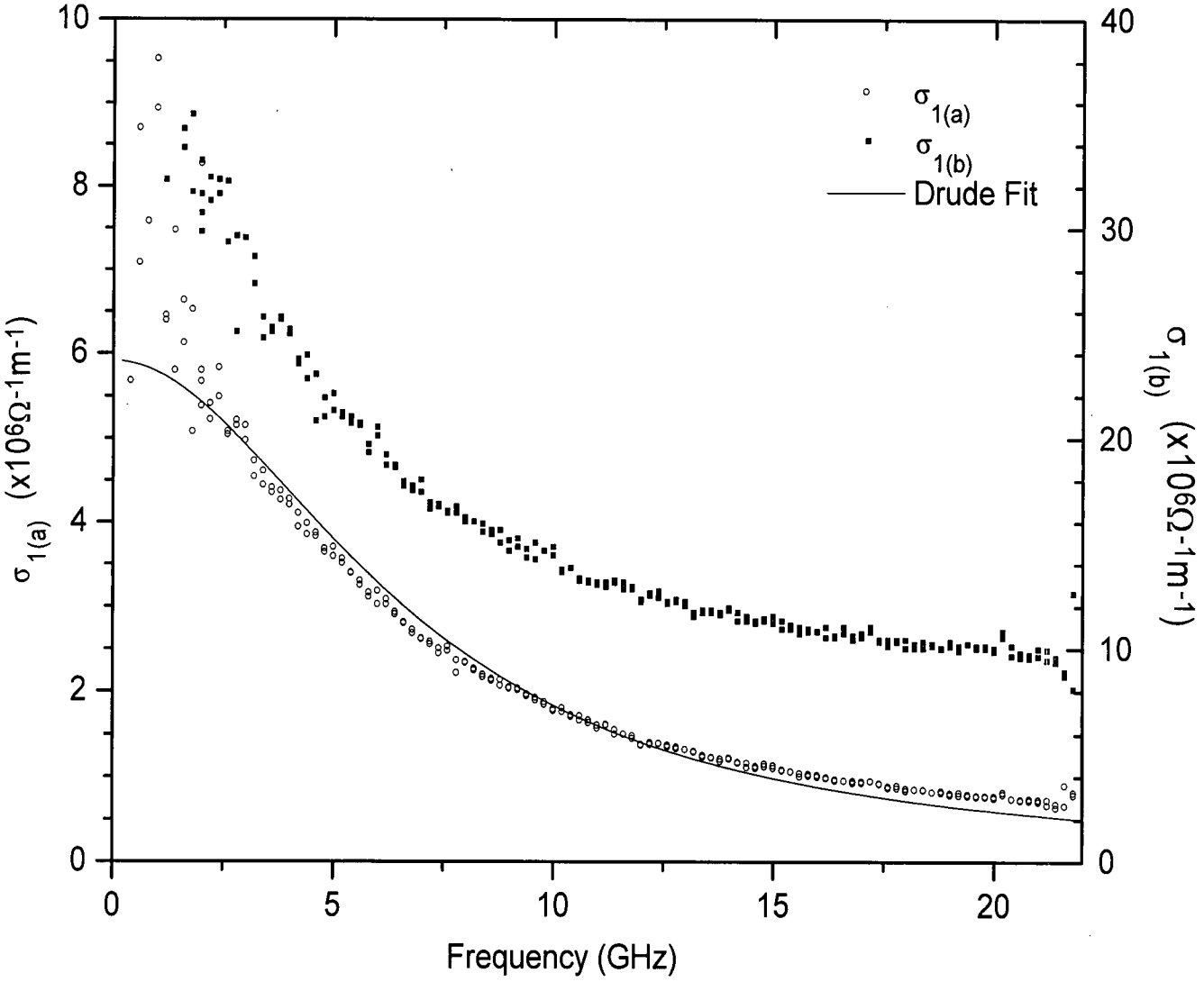

Figure 4.6: $\hat{a}$ and $\hat{b}$-axis $\sigma_1(\omega)$ spectra. A Drude fit is made to $\sigma_{1(a)}(\omega)$ which yields a normal fluid oscillator strength of $ne^2/m_n^* = 2.5 \times 10^{17}$ $(\Omega^{-1}m^{-1}s^{-1})$ and a quasiparticle scattering time of $\tau = 2.4 \times 10^{-11}$ s. The fit did not include data below 3 GHz due to the poor S:N in this range.

limit which is a factor of 3 larger than σ_{oo}. One can interpret the data as being that for $T > T^*$ which is consistent with the fact that the quasiparticle oscillator strength has been observed to be linear in temperature down to 1 K. The bolometry data on the crystal YOV points to conclusions similar to those of Hosseini *et al.*, however the high frequency limit in this case is a factor of 2 larger than σ_{oo}. Further testing of universal conductivity by microwave techniques is necessary in order that the postulated theory be convincingly tested.

The existing measurements on YBCO indicate that at 1.3 K a low temperature frequency independent limit has yet to be realized. Whatever the mechanism responsible for the observed conductivity spectrum, the fact that there is a broad feature with a width of approximately 7 GHz leads one to expect that a $T \rightarrow 0$ limit will be achieved below about 0.35 K (7 GHz$\times$h/k_B). It is clear that microwave experiments in this unexplored temperature range will be of interest to the HTSC community, and plans are currently in progress to operate this experiment at 100 mK.

Chapter 5

Conclusions

The primary goal of this thesis was to develop a highly sensitive bolometric technique to measure the microwave surface resistance of HTSC single crystal samples near 1 K. It has been demonstrated that the technique is operational, permitting the measurement of superconducting samples with $R_s \sim \mu\Omega$ over the frequency range 3-22 GHz.[1] This technique measures the absolute microwave loss of a material, with an uncertainty of 10% due to calibration uncertainties, particularly the determination of the reference alloy's resistivity ρ.

Variations at the level of a factor of two were observed between measurements which call into question the stability and contamination of the YBCO crystal surfaces. Further investigations are needed to understand which contributions to the loss are extrinsic, and which are intrinsic to the superconductor. Given that microwave measurements probe only a thin surface layer of a superconductor, it would not be a surprising discovery that the residual loss is highly sensitive to the quality of the surface.

When analyzed within a generalized 2-fluid model, the broadband bolometry data from the measurement believed to be the most representative of intrinsic behaviour yielded a scattering time $\tau = 2.4 \times 10^{-11}$s and normal fluid oscillator strength $ne^2/m_n^* = 2.5 \times 10^{17}$ $(\Omega^{-1}m^{-1}s^{-1})$ which were found to be consistent with the spectroscopy picture inferred from cavity perturbation data by Hosseini *et al.* After we have established that intrinsic properties are in fact being measured, further investigation of the low

[1]This discounts the region 0.01 GHz < f < 3 GHz where the S:N ratio becomes low for very low loss samples.

temperature regime will be carried out. The present goal is to carry out broadband measurements at operating temperatures down to 100 mK. The results will be relevant to the unanswered questions of universal transport and other predictions for low temperature transport in HTSC materials.

Bibliography

[1] J.G. Bednorz and K.A. Műller. *Z. Phys. B*, **64**:189, 1986.

[2] M. Tinkham. *Introduction to Superconductivity.* McGraw-Hill, 1976.

[3] H.K. Onnes. *Leiden Comm.*, (119b, 122b, 124c), 1911.

[4] Cooper L.N. Bardeen J. and Schrieffer J.R. *Phys. Rev.*, (**108**):1175, 1957.

[5] C.C. Tsuei et al. *Phys. Rev. Lett.*, **73**:593, 1997.

[6] A. Mathai et al. *Phys. Rev. Lett.*, **74**:4523, 1995.

[7] W.N. Hardy et al. *Phys. Rev. Lett.*, **70**:3999, 1993.

[8] A. Hosseini et al. *Phys. Rev. B*, **60**:1349, 1999.

[9] A.J. Berlinsky et al. *cond-mat/9908159*, 1999.

[10] M.H. Hettler and P.J. Hirschfeld. *cond-mat/9907150*, 1999.

[11] R. Harris. *Measurement and Analysis of the In-Plane Electrodynamics of* $YBaCuO_{6.993}$ *at Microwave Frequencies.* M.Sc. thesis, University of British Columbia, 1999.

[12] P.A. Lee et al. *Phys. Rev. Lett.*, **71**:1887, 1993.

[13] Louis Taillefer et al. *Phys. Rev. Lett.*, **79**:483, 1997.

[14] D.A. Bonn et al. *Phys. Rev. B*, **47**:11314, 1993.

[15] J-J Chang and D.J. Scalapino. *Phys. Rev. B*, **40**:4299, 1989.

[16] I. Kosztin and A.J. Leggett. *Phys. Rev. Lett.*, **79**:135, 1997.

[17] D.A. Bonn and W.N. Hardy. In D.M. Ginsberg, editor, *Physical Properties of High Temperature Superconductors, Vol. V*, pages 7–97. World Scientific, 1996.

[18] D.N. Basov et al. *Phys. Rev. Lett.*, **74**:598, 1995.

[19] J. Sonier et al. *Phys. Rev. Lett.*, **72**:744, 1994.

[20] A. Hosseini et al. *Phys. Rev. Lett.*, **81**:1298, 1998.

[21] S. Kamal. *Magnetic Penetration Depth in $YBaCuO_{7-\delta}$*. Ph.D. thesis in preparation, University of British Columbia, 2000.

[22] S. Sridhar and W.L. Kennedy. *Rev. Sci. Instrum.*, **59**:531, 1988.

[23] D.L. Rubin *et al. Phys. Rev. B*, **38**:6538, 1988.

[24] D. Kajfez and P. Guillon. *Dielectric Resonators.* Noble Publishing Corp., 1998.

[25] R.B. Stephens. *Phys. Rev. B*, **8**:2896, 1973.

[26] R.C. Zeller and R.O. Pohl. *Phys. Rev. B*, **4**:2029, 1971.

[27] R.Q. Fugate and C.A. Swenson. *J. Appl. Phys.*, **40**:3034, 1969.

[28] O.V. Lounasmaa. *Experimental Principles and Methods Below 1K.* Academic Press, 1974.

[29] L.C. Jackson F.E. Hoare and N. Kurti. *Experimental Cryophysics.* Butterworths, 1961.

[30] P. Horowitz and W. Hill. *The Art of Electronics.* Cambridge Univ. Press, 1980.

[31] R. Liang et al. *Physica C*, **304**:105, 1998.

[32] R. Liang et al. *Physica C*, **195**:51, 1992.

[33] A. Erb et al. *Physica C*, **245**:245, 1995.

[34] A. Erb et al. *Physica C*, **258**:9, 1996.

[35] A. Erb et al. *J. Low Temp. Phys.*, **105**:1023, 1996.

[36] G.K. White. *Experimental Techniques in Low-Temperature Physics.* Clarendon Press, 1979.

[37] A.A. Abrikosov. *Fundamentals of the Theory of Metals.* North Holland, 1988.

[38] J.M. Ziman. *Principles of the Theory of Solids.* Cambridge University Press, 1972.

[39] J.D. Goldsmith. *Bulletin of Alloy Phase Diagrams*, **1**:45, 1980.

[40] E. Hoskinson. *The Effect of Polishing on the Microwave Surface Resistance Properties of the High Temperature Superconductor $YBa_2Cu_3O_7$*. Undergraduate thesis, University of British Columbia, 1999.

[41] A.C. Durst and P.A. Lee. *cond-mat/9908182*, 1999.

Appendix A

Integration of Ampere's Law

The differential form of Ampere's law reads

$$\nabla \times \mathbf{H} = \mathbf{J}. \tag{A.1}$$

where $\mathbf{H}$ is the external magnetic field and $\mathbf{J}$ is the surface current density (A/m^2). $\mathbf{H}$ and $\mathbf{J}$ are perpendicular. Integrating this over an area of the surface of a semi-infinite plane, and subsequently invoking Stoke's theorem to convert the curl integral to a line integral yields

$$\oint \nabla \times \mathbf{H} \cdot d\mathbf{S} = \oint \mathbf{J} \cdot d\mathbf{S} \tag{A.2}$$

$$\oint \mathbf{H} \cdot d\ell = J_s \cdot \ell. \tag{A.3}$$

where J_s is a surface current per unit width (A/m) and ℓ is the length along the surface. The integration path for $\mathbf{H}$ is chosen to be a loop runing from deep inside the conductor where the field is zero perpendicularly up to the surface and extending a length ℓ along the surface, returning perpendicularly again deep into surface. In this case the integral only picks up the tangential field at the surface where $\mathbf{H}$ is parallel to $d\ell$ and we have

$$H_{\text{tangential at surface}} \cdot \ell = J_s \cdot \ell \tag{A.4}$$

$$H_{yo} = J_{so}. \tag{A.5}$$

Appendix B

J.P.L. Sapphire Cleaning Procedure

This procedure is standard protocol in the lab for the cleaning of sapphire to reduce dielectric losses.

Begin with a cleaned teflon basket to hold sapphire with while immersing in the various solvents.

1. Boil in 1 part H_2SO_4 mixed with 3 parts deionized water for at least 2 minutes.
2. Rinse with deionized water. (This is a UBC added step)
3. Boil in deionizied water for 5 minutes.
4. Rinse with high grade acetone.
5. Boil in high grade acetone for 5 minutes.
6. Rinse with propanol.
7. Boil in propanol for 5 minutes.
8. Rinse with high grade ethanol.
9. Boil in high grade ethanol for 5 minutes.

Some users prefer to blow the sapphire off with dry nitrogen between steps. Following cleaning, handle sapphire only with waxed weighing papers which do not contaminate the surface.

Appendix C

Thin Limit Correction Factor

Consider a semi-infinite slab of metal of thickness t with a magnetic field oriented parallel to the surface. The screening current will flow in opposite directions on the two faces of the metal, and will have a value of J_o at the surface. The current density $J(z)$ will decay exponentially with penetration into the metal, having the general form

$$J(z) = A_1 e^{-\frac{z}{\delta}} + A_2 e^{\frac{z}{\delta}}. \tag{C.1}$$

The boundary conditions require that

$$\begin{aligned} J(\frac{t}{2}) &= J_o \\ J(-\frac{t}{2}) &= -J_o. \end{aligned} \tag{C.2}$$

and from this C.1 becomes

$$J(z) = J_o \left[\frac{\sinh(\frac{z}{\delta})}{\sinh(\frac{t}{2\delta})} \right]. \tag{C.3}$$

The total power absorbed by the metal will depend on the total integrated current density

$$\int_{\frac{-t}{2}}^{\frac{t}{2}} J(z)^2 dz. \tag{C.4}$$

Since

$$\int \sinh^2(ax)dx = \frac{1}{4a}\sinh(2ax) - \frac{x}{2}, \tag{C.5}$$

the total power absorption is given by

$$\int_{\frac{-t}{2}}^{\frac{t}{2}} J(z)^2 dz = \delta \left[\frac{\sinh\left(\frac{t}{\delta}\right) - \frac{t}{\delta}}{\cosh\left(\frac{t}{\delta}\right) - 1} \right]. \tag{C.6}$$

In the thick limit ($\delta \ll t$) the integrated value of the current density is simply δ for two faces. Hence the ratio of the power absorption between the thin and thick limits is given by the factor

$$\frac{P_{thin}}{P_{thick}} = \left[\frac{\sinh\left(\frac{t}{\delta}\right) - \frac{t}{\delta}}{\cosh\left(\frac{t}{\delta}\right) - 1}\right]. \tag{C.7}$$